APPROVAL SHEET

Title of Dissertation: *Miniaturized probes for cell microenvironment: development, characterization, and application of fluorescent oxygen-sensing microparticles*

Name of Candidate: Miguel A. Acosta

Doctor of Philosophy, 2011

Dissertation and Abstract Approved: _____

Jennie B. Leach

Assistant Professor

Chemical & Biochemical Engineering

Date Approved: _____

CURRICULUM VITAE

Name: Miguel A. Acosta

Degree and date to be conferred: Ph.D., 2011

Collegiate institutions attended: B.S.; University of Puerto Rico, Mayagüez; Chemical Engineering

Ph.D.; University of Maryland, Baltimore County; Chemical & Biochemical Engineering

Publications

Journal Publications:

1. M.A. Acosta, Katelyn M. Williams, and J.B. Leach. "Fluorescent silica particles for monitoring oxygen levels in three-dimensional cellular structures." *Langmuir* (in preparation).
2. M.A. Acosta, P. Ymele-Leki, Y. Kostov, and J.B. Leach. "Fluorescent microparticles for sensing cell microenvironment oxygen levels within 3D scaffolds." *Biomaterials* 30, pp. 3068-3074 (2009).

Conference Proceedings:

1. M.A. Acosta and J.B. Leach. "Fluorescent microparticles for sensing cell microenvironment oxygen levels within 3D scaffolds." *Proceedings of the Southern Biomedical Engineering Conference*. (2010) Annual Meeting, University of Maryland College Park, College Park, MD.

2. M.A. Acosta, Y. Kostov, and J.B. Leach. "Microfluidic bioreactors as tools for monitoring cell microenvironment." *Transactions of the 32nd Annual Meeting of the Society for Biomaterials* 30:56, (2007) Annual Meeting, Chicago, IL.

Other Publications:

1. M.A. Acosta, Y. Kostov, and J.B. Leach. "Microfluidic bioreactors as tools for monitoring cell microenvironment." *Revista Científica del Colegio de Químicos de Puerto Rico – El Crisol* 1 (2007), pp. 14-15.

Presentations

National & International Meetings:

1. M.A. Acosta S. Ostrand-Rosenberg, and J.B. Leach. "Fluorescent microparticles for sensing cell microenvironment oxygen levels within 3D scaffolds." *American Institute of Chemical Engineers (AIChE) Annual Meeting*, Salt Lake City, UT; November 2010.
2. M.A. Acosta and J.B. Leach. "Fluorescent microparticles for sensing cell microenvironment oxygen levels within 3D scaffolds." *Southern Biomedical Engineering Conference*, University of Maryland College Park, College Park, MD; May 2010.
3. M.A. Acosta and J.B. Leach. "Fluorescent microparticles for sensing cell microenvironment oxygen levels within 3D scaffolds." *American Institute of Chemical Engineers (AIChE) Annual Meeting*, Nashville, TN; November 2009.

4. M.A. Acosta, Y. Kostov, and J.B. Leach. "Miniaturized probes for cell microenvironment: Development and characterization of fluorescent oxygen-sensing microparticles." *American Institute of Chemical Engineers (AIChE) Annual Meeting*, Philadelphia, PA; November 2008.
5. M.A. Acosta, Y. Kostov, J.B. Leach. "Microfluidic Bioreactors as Tools for Monitoring Cell Microenvironment." *Society for Biomaterials Annual Meeting*, Chicago, IL; April 2007.

Local Meetings:

1. M.A. Acosta, Y. Kostov, and J.B. Leach. "Miniaturized Probes for Cell Microenvironment: Development and Characterization of Fluorescent Microparticle Oxygen Sensors." *Third Annual PROMISE Research Symposium*, University of Maryland, College Park; January 2008.
2. M.A. Acosta, Y. Kostov, and J.B. Leach. "Miniaturized Probes for Cell Microenvironment: Development and Characterization of Fluorescent Microparticle Oxygen Sensors." (Poster) *Look Ahead XI*, UMBC; November 2007.
3. M.A. Acosta, Y. Kostov, and J.B. Leach. "Microparticle oxygen sensors: Miniaturized probes for cellular microenvironment in 3D cultures." (Poster). UMBC – *Wyeth Research Summit*; August, 2007.
4. M.A. Acosta, Y. Kostov, and J.B. Leach. "Miniaturizing oxygen-sensing technologies for microscale tissue engineering applications." *Graduate Research Conference*, UMBC; April 2007.

5. M.A. Acosta, Y. Kostov, and J.B. Leach. "Microfluidic Bioreactors as Tools for Monitoring Cell Microenvironment." (Poster) *Second Annual PROMISE Research Symposium*, University of Maryland, College Park; January 2007.
6. M.A. Acosta, Y. Kostov, and J.B. Leach. "Microfluidic Bioreactors as Tools for Monitoring Cell Microenvironment." (Poster) *Look Ahead X*, UMBC; November 2006.

Professional positions held

1. Research Assistant; Department of Chemical & Biochemical Engineering, University of Maryland, Baltimore County, Baltimore, MD 2005-2011.

ABSTRACT

Title of document: *Miniaturized probes for cell microenvironment: development, characterization, and application of fluorescent oxygen-sensing microparticles*

Miguel A. Acosta, Ph.D. 2011

Directed By: Jennie B. Leach, Ph.D.
Assistant Professor
Chemical & Biochemical Engineering
University of Maryland, Baltimore County

Oxygen concentration is a key parameter in tissue culture and tissue engineering. As such, oxygen diffusion through biomaterials plays an important role in maintaining healthy tissues. As such, oxygen is one of the most important cues within the cell microenvironment, playing a role in the regulation of cellular responses that concern such cellular phenomena as cell migration, proliferation, and apoptosis. Oxygen supply has become a limiting factor during the growth of highly metabolic tissues and large tissue masses, mainly as a result of insufficient vascularization and the low aqueous solubility of oxygen. In addition, limited oxygen supply has been linked to the propagation of bacterial infections due to bacterial detachment from biofilms within the body. Therefore, gaining an understanding of

the cellular response to changes in soluble cues, such as oxygen concentration, through their microenvironment may potentially lead to optimized oxygen delivery within biomaterials, improved methods to control cell behavior in engineered tissues, and improved therapies to treat bacterial infections. However, mapping oxygen concentration and characterizing oxygen transport in three-dimensional culture systems has proven difficult due to the lack of adequate tools.

To address this need, we have developed oxygen-sensing microparticles that can be suspended through the volume of a transparent biomaterial and measure oxygen concentration and characterize oxygen transport in a non-invasive manner. These microparticles sense oxygen by fluorescence quenching of the oxygen-sensitive fluorophore tris (4,7-diphenyl-1,10-phenanthroline) ruthenium (II) dichloride, or $Ru(Ph_2phen_3)Cl_2$, while immobilized onto silica carriers. These microparticles are geared towards applications in both mammalian and bacterial cell culture where oxygen concentration and transport can be directly correlated to cell function. We provide a detailed description of the synthesis processes of these microparticles, their characterization, and calibration. Subsequently, we show that they are suited for their intended applications by demonstrating that they can be suspended through the volume of a biomaterial and are compatible with both mammalian and bacterial culture. Finally, we propose methodologies for the intended applications of the microparticles regarding the correlation cell function to oxygen transport during 3D mammalian cell culture and bacterial biofilm culture. This correlation will mark the first time oxygen concentration is linked to cellular functions that it directly impacts during three-dimensional culture.

Miniaturized probes for cell microenvironment: development, characterization, and application of fluorescent oxygen-sensing microparticles

By

Miguel A. Acosta

Dissertation submitted to the Faculty of the Graduate School of the University of Maryland, Baltimore County, in partial fulfillment of the requirements for the degree of Doctor of Philosophy, 2011

ACKNOWLEDGEMENTS

First and foremost, I would like to thank my advisor Dr. Jennie Leach, for her great patience, unconditional support, and her willingness to take part in my professional and personal development. Secondly, I would like to extend my gratitude to my committee members Dr. Julia Ross, Dr. Theresa Good, Dr. Douglas Frey, and Dr. Suzanne-Ostrand Rosenberg for their continued supports and advice. In particular, I would like to extend my appreciation towards Dr. Ross and Dr. Rosenberg for allowing me to be part of their laboratories and to conduct my work in conjunction with their members. Thirdly, I would like to thank Dr. Renetta Tull, also for her unconditional involvement in my professional growth and for her continued support in the many other facets of my stead at UMBC.

Additional gratitude goes towards Dr. Yordan Kostov, for training me in the many techniques that would become a mainstay throughout the course of my work, and towards Dr. Patrick Ymele-Leki, for his continued involvement in my work and in the development side projects that would later turn out to be great additions to the completion of my dissertation. Also, I extend my thanks to Dr. Charles Bieberich and Laura Mutton in the department of Biological Sciences for their invaluable assistance with.

Much gratitude is extended towards my past and present laboratory members Silviya Zustiak, Andreia Ribeiro, John Van Druff, Swarnalatha Balasubramanian, and Yunqian Wei for their continued support. Special consideration goes to Andriea Ribeiro for being more than just co-worker, a magnificent friend. Additionally, much gratitude is extended towards the undergraduate members of our laboratory; in

particular, to Melissa Velasquez and Katelyn Williams for their hard work in the progression of my projects.

I would like to extend my thanks to the members of the graduate student community of the Chemical & Biochemical Engineering department and the Rosenberg laboratory in the department of Biological Sciences for their support and their involvement in my career as a graduate student. Especial acknowledgements go to Bill Moss for being my best friend through the course of this process.

I would like to thank Victor Fulda for his hard work in propelling our ideas, maintaining the department afloat with his hard work, and for his continued support of all the graduate students. Many thanks as well to department staff members Mary Anderson and Denise Kedzierski for their aid in resolving all matters regarding the bridging of the graduate student community and the department.

Finally, I extend my sincere gratitude to the community of the Academy of Traditional Fighting Arts for their continued involvement and interest in my personal growth. Last but not least, my deepest and most heartfelt gratitude goes to my partner Christine Franey for being a true friend and partner, for her light guided my way through this process and I hope it continues to do so wherever my future endeavors may take me.

TABLE OF CONTENTS

LIST OF TABLES

LIST OF FIGURES

CHAPTER 1: Background

1. Motivation and summary of work

Understanding the mechanisms underlying cell response to cues from their biomaterial microenvironment will ultimately lead to improved methods for control over cell behavior in tissue replacement therapies [1]. Whereas many methods have been established for the characterization of cellular behavior and the physical properties of biomaterial scaffolds, few methods exist for directly measuring the spatial fluctuations of soluble cues that impact cellular function. Only in recent years, with the advent of new microscale technologies (e.g. microfluidics and bio-micro-electromechanical systems, or Bio-MEMS), have scientists developed the proper tools to quantify the cellular response to specific stimuli. For example, Gunawan et al. utilized microfluidics to study cell migration in response to gradients in extracellular matrix (ECM) proteins [2]. Studies such as these, where cell response is investigated with the aid of new and inventive tools, help expand our knowledge of cellular behavior and provide design rules for engineering new biomaterials that can control cell behavior.

Oxygen is one of the critical parameters that affect cell viability (along with pH, temperature, and nutrient supply). Additionally, oxygen concentration itself is one of the cues that directly impacts cell response. For example, new vasculature grows into tissue regions that have low oxygen content. This process, angiogenesis, occurs as a result of the cascade of cellular signals and responses initiated upon the

cells' sensing of the decreased oxygen concentration, due to consumption and/or poor delivery. The new vasculature in turn improves oxygen and nutrient delivery to tissues via blood flow. Measuring oxygen concentration throughout the volume of laboratory scale tissue culture systems is a difficult task because traditional oxygen-sensing approaches are not amenable to miniaturization. Moreover, oxygen-sensing electrodes also consume oxygen available to cells during operation. With the advent of the optical sensor technologies based on fluorescence quenching, measurements of oxygen concentrations during cell culture can now be carried out in a reliable and noninvasive manner.

The work presented, focuses on the development, characterization, and application of oxygen-sensing microparticles based on fluorescence quenching of the oxygen-sensitive fluorophore tris (4,7-diphenyl-1,10-phenanthroline) ruthenium (II) dichloride, or $Ru(Ph_2phen_3)Cl_2$. By monitoring the fluorescence quenching of the oxygen-sensitive fluorophore using a fluorescence microscope, measurements of both temporal and spatial changes in oxygen concentration can be carried out in a non-invasive manner without consuming the oxygen available to the cells during culture. These sensing microparticles are uniquely suited to allow micron-scale high resolution, real-time correlations between oxygen concentration and cell response in three-dimensional systems, such as tissue engineering scaffolds. The microparticles are synthesized by a simple and inexpensive two-step process, yielding fluorescent microparticles that can be suspended in any transparent substrate or scaffold used in laboratory scale cell culture. Additionally, the versatility of the governing chemistry allows for adaptations of the particles better suited for applications with size and

emission range constraints. Their simple preparation and ease of use makes them a valuable option for tissue engineers and cell biologists without requiring advanced knowledge of optics or electronics.

The topics that will be specifically discussed in this thesis concern the following: (1) the development of the oxygen-sensing microparticles and the characterization of their properties (e.g. size, cytotoxicity, reversibility, and calibration) (Chapter 2); (3) optimization of the particle synthesis process towards the development of particles in a smaller size range, better suited for applications concerning bacterial biofilms (Chapter 3); and (4) the application of the microparticles towards the correlation of tumor cell response to hypoxia during 3D culture (Chapter 4).

In the following sections, the reader will find introductory remarks regarding some of the concepts that govern the aforementioned topics, to be described in subsequent chapters. We begin with an introduction to the oxygen's role in cell culture and tissue engineering and follow with an introduction to the effects of hypoxia (low oxygen concentration) on bacterial infections. We then describe the hypoxia-inducible factor-1 and its relationship to hypoxic cell response and cancer, and we propose the use of its α-subunit as a target molecule for correlating oxygen concentration and cell response. Next, oxygen diffusion through biomaterials and the phenomenon of fluorescence quenching and its applications in oxygen sensor technologies are introduced. Finally, we introduce the Stöber synthesis, describe its applications in chemistry and biotechnology, and overview its application

combination with fluorescence quenching technology for the development of micron-sized oxygen sensors.

2. Role of oxygen in cell culture and tissue engineering

Oxygen constitutes approximately 20% of the dry weight of cells and is present in all organic cellular components. Molecular oxygen is also required in the aerobic metabolism of carbon compounds for the production of ATP – a process known as oxidative phosphorylation [3]. Furthermore, low oxygen concentration in the cell microenvironment influences the transition from aerobic to anaerobic metabolism, where mammalian cell function and viability are compromised. Thus, oxygen concentration is a key parameter in cell culture. In addition, oxygen diffusion through biomaterial scaffolds plays an important role in maintaining healthy tissues cultured in vitro, as oxygen supply becomes a limiting factor during the culture of highly metabolic tissues and tissue masses with thicknesses above 100 μm. This is mainly a result of the lack of vascularization in tissues cultured in vitro and the low solubility of oxygen in the culture medium, as an oxygen molecule only diffuses ~100 μm away from the surface of a tissue construct before it is consumed [4]. As a consequence of these limitations, cells at the surface of large tissue constructs are usually viable, whereas cells at the center of the construct are hypoxic and necrotic.

Numerous studies have attempted to correlate oxygen concentration to the success of engineered tissues. For example, Radisic et al. demonstrated that oxygen diffusion is a limiting factor during the culture of 1.5 mm-thick cardiac tissue constructs [5]. In their study, levels of α-actin, troponin-1, and connexin-43 were

reported to decrease at the center of the tissue construct, where the cells are experiencing hypoxia (Figure 1). The proteins α-actin, troponin-1, and connexin-43 are related to the contractile behavior of cardiac myocytes and are associated with physiological behavior. In another study, Tilles et al. developed a microchannel bioreactor with a built-in membrane oxygenator and demonstrated that improved oxygen delivery enhanced hepatocyte albumin and urea synthesis by > 1300% and > 500% respectively, in comparison to cultures without a membrane oxygenator [6]. Albumin constitutes approximately 60% of the proteins in human plasma and urea, although primarily a waste product, plays an important role in kidney function. Both molecules are produced in the liver and are indicators of healthy hepatocyte function during culture in vitro. These studies highlight how cell viability and function are compromised by hypoxia.

Oxygen concentration also plays a significant role in other cellular phenomena, such as chondrogenesis (production of new cartilage) in vitro, angiogenesis (production of new blood vessels) in vivo, and the propagation of diseases, such as cancer. For instance, chondrogenesis has been demonstrated to be maximal in the oxygen partial pressure range of 19-24 mm Hg (normoxic), but inhibited in the low (hypoxic) 1.6-8 mm Hg and the high (hyperoxic) 143-160 mm Hg ranges [7]. Hypoxia has been demonstrated to play a role in tumor resistance to radiation treatment, whereas hyperoxia can cause cell death via the formation of reactive oxygen species [8-12]. Furthermore, it has been observed that tumors contain regions of severe hypoxia, referred to as anoxia (< 1.6 mm Hg). Under anoxia, cells lie in a state functionally different from that associated with conventional hypoxia,

where protein synthesis and translocation drops dramatically and oxidative stress granulation is observed [13, 14]. Anoxia promotes tumor cell toxicity and apoptotic cell death [15]. Thus, it is evident that oxygen plays an important role in cellular function and that understanding of the mechanisms underlying cell response to changes in oxygen concentrations in the cell microenvironment can ultimately lead to biomaterial scaffolds that direct cellular behavior, as well as improved therapies for cancer and other diseases.

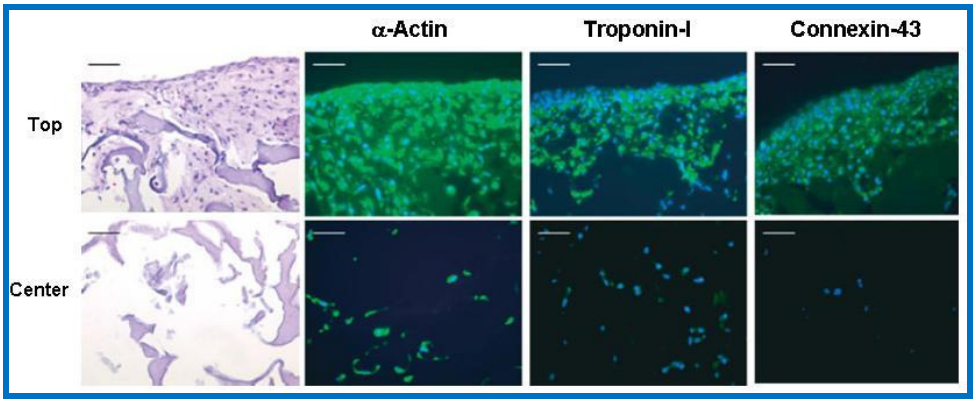

Figure 1: Tissue morphology and expression of cardiac markers α-actin, troponin-1, and connexin-43 at top surface and center of 1.5 mm-thick cardiac tissue construct. The three proteins were stained with fluorescein (green) and cell nuclei were stained with 4',6-diamidino-2-phenylindole (DAPI, blue). Here, the expression of α-actin, troponin-1, and connexin-43 proteins at the surface and the bottom of the tissue construct is compared. The results show healthy cellular function at the surface of the tissue, whereas the cells at the bottom are predominantly dead. Scale bar = 50 μm. Figure adapted from Radisic et al [5].

Unfortunately, the majority of studies that attempt to correlate oxygen concentration directly to cell response have relied on probe measurements of one area of a sample or on mathematical predictions of oxygen diffusion and consumption.

Hence, studies in this area have been hindered by the lack of available tools to quantitatively measure or map oxygen concentration through 3D systems and simultaneously correlate it to cell response.

3. *Staphylococcus aureus biofilms and oxygen diffusion*

Staphylococcus aureus is a bacterial pathogen responsible for many cases of hospital-acquired infections, such as those related to prosthetic device implantations [16]. *S. aureus* infections have proven difficult to treat due to their ability to form organized biofilms [17], which contribute to antibiotic resistances [18, 19], and secondary metastatic infections caused by free flowing planktonic-cells that detach from the biofilms [20]. The complex structure of the biofilm and its internal channels are poorly understood, as are the nutrient and oxygen transport dynamics through the volume of the biofilm that influence the cells. For example, Cramton et al. demonstrated that anoxic conditions inside the volume a biofilm promote the production of polysaccharide intercellular adhesin (PIA), which is a key molecule responsible for promoting biofilm formation and growth [21]. This suggests that the presence a biofilm further increases the incidence of biofilm formation. Additionally, increased PIA expression may also impair the penetration of antibiotics in biofilms. Thus, more complete understanding of not just the mechanisms behind biofilm formation, proliferation, and planktonic-cell detachment, but also an understanding of oxygen transport through the volume of a biofilm is vital for the development of new and effective infection therapies.

Whereas a few studies have treated planktonic-cell adhesion to substrates and biofilm proliferation, much is still unknown about regarding oxygen transport through the volume of the biofilms and how it affects its formation and metastasis. As with studies that have attempted to correlate oxygen concentration to mammalian cell response, progress on the understanding of oxygen transport and biofilm behavior has been hindered by the lack of adequate tools to map oxygen and nutrient transport through biofilms. The major challenges posed by biofilms towards the study of oxygen transport come primarily from their size. *S. aureus* cells are roughly 1 μm in diameter, and with biofilms being composed of several layers of bacterial cells, oxygen-sensing technologies on the same size scale as bacteria are required to map their internal oxygen profiles.

4. Hypoxia-inducible factors-1 (HIF-1) and -1α (HIF-1α)

HIF-1 is a heterodimer composed of HIF-1α and HIF-1β subunits, both of which are helix-loop-helix transcription factors [22]. HIF-1β (91-94 kDa) is a nuclear protein that is constitutively expressed in a manner independent of oxygen concentration. Conversely, HIF-1α (120 kDa) is a cytoplasmic protein and its regulation is dependent on oxygen concentration [22, 23]. Under normoxic conditions, HIF-1α is continuously degraded by the ubiquitin-proteasome system. However, under hypoxic conditions, HIF-1α is transferred to the nucleus where it combines with HIF-1β to form HIF-1, which binds to hypoxia response elements (HRE) present in genes to activate transcription [22, 23]. These genes encode for

proteins involved with erythropoiesis, angiogenesis, glycolysis, cell proliferation, apoptosis, and many others functions [22, 23].

Thus, HIF-1α is a well-established target molecule for directly correlating cellular function with oxygen concentration. Measurements of HIF-1α may be considered direct, as they provide a better insight into how cells mediate their response to hypoxia and specific oxygen concentrations that regulate these processes. HIF-1α has also been linked to various diseases, including cancer, where its levels inside tumors can be directly correlated to tumor hypoxia [24]. Tumor hypoxia activates the HIF-1 pathways that lead to angiogenesis and other functions. Hence, as tumors increase in size they develop their own vascular networks with the aid of HIF-1. Newly formed blood vessels around the tumors, however, suffer from structural and functional abnormalities that limit proper nutrient and oxygen delivery [22, 25]. It is through these connections between tumor and host vasculature that cells escape the hypoxic tumor microenvironment, promoting metastasis [26]. For this reason, it has been suggested that possible cancer therapies may involve the inhibition of HIF-1 and HIF-1α activity [23, 26-28]. Therefore, HIF-1α regulation by tumor cells is an important and well-established biological system to test the utility of the oxygen-sensing technologies for correlating oxygen concentration to cellular behavior in 3D cultures.

5. Oxygen diffusion through biomaterials and tissues

Significant efforts have been directed towards optimizing oxygen delivery during the culture of highly metabolic tissues, as well as understanding oxygen

diffusion through native and engineered tissue systems. Two examples are: (1) the addition of oxygen carriers to the culture medium that will increase oxygen solubility and delivery, such as fluorocarbons and erythrocytes from bovine blood, and (2) the modeling of oxygen transport through engineered heart tissues [29-32]. However, fewer efforts have been placed on understanding oxygen transport in commonly utilized biomaterial scaffolds without the inclusion of cells. This aspect is equally as important as understanding oxygen transport through tissues, for it can lead to the engineering of better biomaterial scaffolds that can provide improved oxygen delivery. Moreover, scaffolds could potentially be engineered to provide control over cell behavior by the formation of stable gradients in oxygen concentration.

Oxygen diffusion studies have been conducted for some of the more common natural and synthetic hydrogel materials, such as alginate, agarose, poly(ethylene glycol) (PEG), and poly(2-hydroxylethyl methacrylate) (poly-HEMA) [33-38]; out of which, poly-HEMA has the largest available literature due to its commercial success as a component in contact lenses. Nonetheless, poly-HEMA is seldom used in cell culture and its effective oxygen diffusivity is too low, in comparison to that of the other mentioned materials, to meet cell culture demands (D_e = 1.36 x 10^{-7} cm^2/s [39], which is < 1% of the effective oxygen diffusivity through water). Hydrogels can hold > 90% water; hence, it has been common practice to compare their effective oxygen diffusivities (D_e) to that of oxygen through water (D_0) in the form of the ratio D_e/D_0. Studies have demonstrated that oxygen diffusion is influenced by hydrogel concentration, being reduced to as low as 25% that of oxygen through water (D_e/D_0 = 0.25) [38]. Table 1 lists examples of oxygen effective diffusivities for several types of

hydrogels. Unfortunately, most of the studies listed in Table 1 treat the combined cell culture and biomaterial system, which is very complex, and place no emphasis on potential modifications that could be made to the biomaterial to improve oxygen transport through their system.

Studies that have measured oxygen concentrations in cultured tissues have utilized a wide range of techniques (examples are listed in Table 2). Although there are techniques available that can provide information about either oxygen concentration or cellular response to hypoxia independently (e.g. optical sensors and electrodes for measuring oxygen concentrations and assays that quantify metabolic activity and protein expression, such as MTT and ELISA), a methodology that can bring both aspects together is yet to be established.

Table 1: Reported values of normalized effective oxygen diffusivity (D_e/D_0) for various hydrogel compositions.

Material	Concentration (w/v)	D_e/D_0	Reference
Ca-Alginate	1%	0.64	[34]
	1.5%	0.53	[35]
	2%	0.73	[34]
		0.92	[36]
		0.86	[37]
	3%	0.66	[34]
		0.45	[35]
	4%	0.84	[37]
Ba-Alginate	2%	0.54	[36]
		0.25	[38]
Agarose	2%	0.95	[34]
		1.0	[35]
	4%	1.0	[35]
	5%	0.73	[34]
	8%	0.62	[34]
PEG	0.5%	0.98	[33]
	1%	0.93	[33]
	1.5%	0.91	[33]
	2%	0.86	[33]

Table 2: Examples of previous studies that have attempted to correlate cell function and oxygen concentration.

Method	Systems	References	Comments
Modeling	1. 1.5 mm-thick constructs of rat cardiac myocytes cultured in collagen. 2. 1.2 mm-thick constructs of rat myocytes cultured in collagen-Matrigel mix. 3. Bovine chondrocytes cultured in PEGT/PBT (polyethylene glycol terephthalate/polybutylene terephthalate) copolymer matrices. 4. C3A hepatoma cells culture in hollow fiber bioreactor. 5. Rat cardiac myocytes cultured in poly(glycerol sebacate) (PGS) constructs house inside a parallel-channel array perfusion system. 6. 15-60 mm-diameter poly(lactic-co-glycolic acid) (PLGA) dome-shaped scaffolds with base blood vessel loop using mathematical models for cell growth rate, oxygen uptake rate (OUR), cell volume, cell migration, and capillary growth rate. 7. Rat hepatocytes cultured in collagen inside flat-plate bioreactor.	[5] [31] [40] [41] [42] [43] [44]	Mathematical modeling of oxygen transport and consumption. Cellular response to hypoxia evaluated qualitatively only, or not at all. Oxygen measurements carried out with Clark-type electrodes which consume oxygen during operation.
Pimonidazole hydrochloride as a marker for hypoxia alone and in combination with optical sensors	1. 5 μm frozen sections of human squamous cell carcinomas of the larynx implanted on mice. 2. EMT6-Ed spheroids 3. 5 μm frozen sections of human squamous cell carcinomas of the larynx and human glioblastomas implanted on mice.	[45] [46] [9]	Pimonidazole hydrochloride is an intracellular marker of hypoxia. Only identifies hypoxic areas in tissues. Provides no quantitative information of the oxygen concentrations in the environments outside the cell. Provides no quantitative information regarding the cellular response to hypoxia (i.e. what cellular processes are activated under hypoxic conditions). Fiber optic probes are only capable of measuring in their immediate point of contact and surrounding area.

Optical Sensors only	1. Bovine chondrocytes cultured in 5 mm-diameter and 2 mm-thick poly(glycolic acid) (PGA) scaffolds immobilized on top of Pt-porphyrin foils with 0.5% Ca-alginate gels. 2. Bioluminescence imaging of luciferase transfected 9L rat glioblastoma with a commercial fiber optic probe.	[47] [48]	Optical sensor foils only capable of measuring at the surface of histological sections. Incapable of providing information regarding cellular response to hypoxia and measuring in 3D. Bioluminescence imaging is dependent on intracellular conversion of luciferin, which in turn is rapidly degraded. Hence, administration of luciferin before each experiment is required.
Magnetic resonance imaging (MRI)	1. Hamster ovary cells cultured on Cytodex 1 beads and loaded onto a hollow-fiber bioreactor.	[49]	MRI only provided qualitative information regarding the distribution of oxygen through the hollow-fibers of the reactor. No in situ measurements conducted. No information regarding cellular response to hypoxia provided.
In vivo imaging	1. Mice bearing EMT6 carcinoma cells injected with albumin-bound Pd-porphyrin and visualized with a custom made light-guide phosphorimeter. 2. Mice bearing RIF-1 cells that had internalized lithium octa-n-butoxy-naphthalocyanine (LiNc-BuO) oxygen-sensitive particles and visualized with electron paramagnetic resonance imaging (EPRI).	[50] [51]	Fluorescence signal from Pd-porphyrin luminophore molecules may be inhibited by albumin binding. Nonetheless, luminophore was injected into bloodstream of tumor-bearing mice (blood serum is ~60% albumin). As with Pimonidazole hydrochloride, lithium probes are for intracellular measurements and provide no quantitative information of the oxygen concentrations in the environments outside the cell.

6. Fluorescence quenching by oxygen

The development of optical oxygen sensors that employ fluorescence quenching spans a wide variety of approaches (summarized in Table 3). Although Clark-type microelectrodes with tip dimensions of up to a few micrometers have been developed [52], they still consume oxygen during operation and remain unsuited for

measurements of oxygen concentration in laboratory scale cell culture systems. Thus, optical sensors based on fluorescence quenching have demonstrated great potential as tools for quantitatively mapping fluctuations in oxygen concentration that impact cell response in laboratory scale cell culture studies. Furthermore, they have been used as tools for characterizing oxygen diffusion in biomaterials [39].

Fluorescence quenching refers to any process that decreases the fluorescence intensity of a fluorophore (Figure 2). It has been studied extensively both as a phenomenon and a means for obtaining valuable information about a system [53]. The quenching of fluorescence can be classified in one of two types: static quenching and dynamic (or collisional) quenching. In static quenching, a non-luminescent ground-state complex between the fluorophore and the quencher is formed when they come into contact. When this complex absorbs light, it immediately returns to its ground-state without emission of a photon and without causing a change in the fluorescence lifetime of the fluorophore [53].

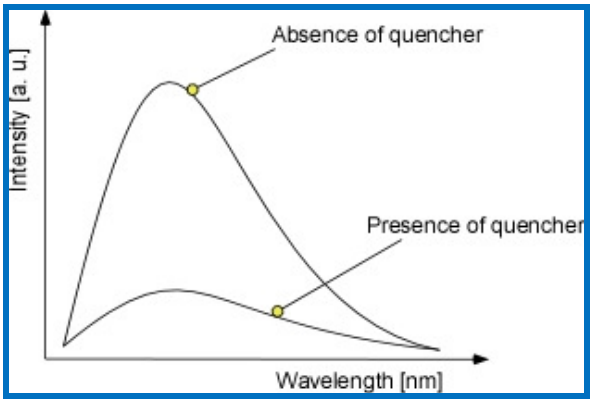

Figure 2: Example of fluorescence quenching. The schematic shows a representation of the change emission intensity of a fluorophore upon exposure to a quencher.

In dynamic quenching, collisions between the fluorophore molecules and the quencher cause energy to be transferred from the excited fluorophore to the quencher, reducing both its fluorescence lifetime and emission intensity. Molecular oxygen is one of the best-known dynamic quenchers [53]. Dynamic fluorescence quenching is described by the Stern-Volmer equation:

$$\frac{I_0}{I} = \frac{\tau_0}{\tau} = 1 + K_{SV}[Q] \quad (1)$$

where I_0 and τ_0 are the fluorescence intensity and lifetime respectively, in the absence of the quencher; I and τ are the fluorescence intensity and lifetime respectively, in the presence of the quencher; K_{SV} is the Stern-Volmer constant; and [Q] is the concentration of the quencher.

James Demas and co-workers pioneered the use of fluorescence quenching by oxygen as a tool for the development of optical oxygen sensors. These sensors were based on transition-metal-complexes of Ru(II), Re(II), and Os(II) [54, 55]. Demas found that these fluorophores were versatile because they are highly quenched by oxygen and can be immobilized in various polymeric materials, such as silicone rubber [56, 57]. In addition, he found that quenching by oxygen of these fluorophores was purely dynamic and that once they were embedded in a polymeric support, experimental data of intensity and lifetime with varying oxygen concentration deviated slightly from the linear model proposed by Equation 1, which corresponds to the fluorophores in solution. These deviations were caused by non-uniform distributions of fluorophore molecules throughout the polymer matrix and could be

taken into account by manipulating the Stern-Volmer model to consider two fluorophore populations, one viable for quenching (or "quenchable") and one not viable for quenching (or "unquenchable") [58].

Table 3: Examples of optical oxygen sensors.

Sensor Format	References	Comments
Nanoparticles	[59]	Nanoparticles, dubbed PEBBLE's, synthesized from various materials such as polyacrylamide, decyl methacrylate (DMA), and organically modified silicate (ORMOSIL). Originally designed for intracellular measurements. Nanoparticles were confirmed to be endocytosed by cells, but effects on cellular activity were not studied. Calibration of nanoparticles was performed outside of the cell, in a system not comparable to its targeted environment.
Sensor patches	[60]	Robust fluorometric sensor patch developed by Govind Rao and co-workers from the UMBC Department of Chemical and Biochemical Engineering. Patch proven to be autoclavable, non-toxic, and fast. Used in High-throughput Bioreactor (HTBR) system for fast optimization of bioprocess parameters. However, sensor patch not designed for measurements in 3D.
Sensor films	[61, 62]	The sensor developed by John et al. consists of poly(dimethylsiloxane) (PDMS) films containing luminophore-bound silica gel. Used for measurements of oxygen concentration during bacterial culture. However, sensor film not designed for measurements in 3D and reference luminophore emission spectrum overlaps with that of oxygen-sensitive luminophore, limiting its application to custom made optical systems only.
Fiber optic microsensors	[63-65]	Fast fiber optic microsensors capable of measuring oxygen, temperature, and pH simultaneously. Minimally invasive. However, fiber optic microsensors still take measurements in their immediate point of contact and surrounding area, limiting its use in 3D.

Regardless, fluorescence quenching has seen great commercial success and has proven to be a valuable tool for measuring oxygen concentrations in bioprocesses and laboratory scale cell culture systems in a reliable and non-invasive manner without consuming oxygen [49, 56, 57]. However, most non-commercial optical oxygen microsensors based on fluorescence quenching make use of custom made electronics for data collection and analysis. This disadvantage creates a barrier

towards adaptation of these sensor platforms by tissue engineers and biomaterial scientists who lack expertise in electronics or photonics.

7. The Stöber synthesis

The Stöber synthesis refers to the hydrolysis and condensation of tetraethylorthosilicate (TEOS) in the presence of water and an alcohol. The reaction can either be base or acid catalyzed (typically by either acetic acid or ammonia) [66-68]. The process yields a colloidal suspension of spherical monodispersed porous silica (SiO_2) spheres between the sizes of 500 nm to 1 μm. The reaction can be described with the following chemical equation [69]:

$$Si(OCH_2CH_3)_4 + H_2O \xrightarrow{\text{Acid or Base}} Si(OH)_4 \xrightarrow{\text{R-OH}} SiO_2 + H_2O \quad (2)$$

where R-OH is a short chain alcohol (usually methanol, ethanol, or propanol).

The process was pioneered by Werner Stöber in 1968 [66] and since, it has seen widespread use for the development of colloidal silica for applications in various fields such as chemistry, biochemistry, optics, electronics, and manufacturing. Two examples include the efforts from Rossi et al. and Nagao et al., who synthesized monodispersed silica particles to serve as carries for sensor molecules in bioassays and as carriers for magnetic nanoparticles, respectively [70, 71]. Furthermore, the versatility of the process' chemistry has allowed for its modification to synthesize monodispersed porous silica particles from analog compounds, such as dimethyldiethoxysilane (DMDES), methyltriethoxysilane (MTES), and 3-

aminopropyltriethoxysilane (APTES) [72, 73], and for the modification of the particles' surface to allow for the detection of molecules of interest, such as the breast cancer marker HER2/neu and trinitrotoluene (TNT) [74, 75]. Additional modifications to the synthesis process have been proposed by Vincent et al., who demonstrated that the addition of surfactants and salts during synthesis can control particle size [72, 73, 76].

It is evident that the Stöber synthesis is a reliable process for producing monodisperse microparticles. It is also versatile, as it has seen many modifications and applications since established. Thus, the particles yielded by this synthesis are perfectly suited for sensor applications that have near sub-micron size constraints, such the study of oxygen transport through *S. aureus* biofilms. The combination of the Stöber synthesis with fluorescence quenching technology could be the ideal course for such studies. In fact, the synthesis of silica microparticles encapsulating a transition-metal-complex of Ru(II) has been performed successfully already [70], further reinforcing the hypothesis that the combination between the two technologies is a suitable approach.

CHAPTER 2: Fluorescent microparticles for sensing cell microenvironment oxygen levels within 3D scaffolds

1. Introduction

Understanding the mechanisms underlying how cells respond to cues from their microenvironment will ultimately lead to improved methods to control cell behavior in tissue replacement therapies. Oxygen concentration is one such cue that directly impacts cell response; a notable example of this effect is the growth of new capillaries into tissue regions that have low oxygen content. Oxygen is required for the aerobic metabolism of carbon compounds, and as such, it is one of the critical parameters (along with pH, temperature, and nutrient supply) that impacts cell viability. Furthermore, hypoxia has been linked with the progression of diseases such as cancer, where it plays a role in tumor resistance to radiation treatment [9, 11, 12], and hyperoxia can cause cell death via the formation of reactive oxygen species [8, 10].

It is well know that oxygen supply becomes a limiting factor during the culture of highly metabolic tissues and tissue masses with thicknesses greater than 100 μm. This is a result of the lack of vascularization in tissues cultured in vitro and the low solubility of oxygen in the culture medium, as an oxygen molecule only diffuses ~100 μm away from the surface of a tissue construct before it is consumed [4]. As a consequence of these limitations, cells at the surface of large tissue constructs are usually viable, whereas cells at the center of the construct are hypoxic and necrotic.

A number of studies have attempted to correlate oxygen concentration to the success of engineered tissues. For example, Radisic et al. demonstrated that oxygen diffusion is a limiting factor during the culture of 1.5 mm-thick cardiac tissue constructs [5]. In their study, levels of α-actin, troponin-1, and connexin-43, which are related to the contractile behavior of cardiac myocytes and are associated with physiological behavior, were reported to decrease at the center of the tissue construct, where the cells were experiencing hypoxia. In addition to cardiac tissue engineering, oxygen concentration has also been explored as a means to modulate chondrogenesis [7] direct stem cell differentiation [44].

Thus, it is evident that oxygen plays an important role in cellular function and that understanding of the mechanisms underlying cell response to changes in oxygen concentrations in the cell microenvironment may ultimately lead to new engineering tools to direct cellular behavior as well as improved clinical therapeutics for a variety of applications. Unfortunately, most studies in three-dimensional constructs have relied on probe measurements of one area of the sample or mathematical predictions of oxygen diffusion and consumption. Although Clark-type microelectrodes with tip dimensions of up to a few micrometers have been developed [52] they still remain unsuited for measurements of oxygen concentration in laboratory-scale tissue engineering systems because they consume oxygen during operation. Hence, studies in this area have been hindered by the lack of experimental tools to quantitatively and non-invasively measure oxygen concentration in three-dimensional systems.

Here, we present the development and characterization of fluorescent oxygen-sensing microparticles that can be suspended in any transparent biomaterial scaffold

used in cell culture and tissue engineering. By monitoring fluorescence quenching of the sensing microparticles with a fluorescence microscope, ratiometric measurements of temporal changes in oxygen concentration can be performed in a rapid, automated, and non-invasive manner without consuming the oxygen available to the cells during culture. Similar sensor technologies have been developed previously, where two recent examples include (1) fluorescent calcium alginate particles surrounded by two polyelectrolyte bilayers for simultaneous measurement of glucose and oxygen concentrations [77], and (2) optical fibers that were modified with a hydrogel matrix containing fluorescent sensor particles for simultaneous measurement of oxygen concentration and pH [78]. In contrast, we focused on a non-cytotoxic micron-scale particle design to allow for application in three-dimensional investigations of the cell microenvironment. This unique combination of biocompatibility, size, sensitivity to oxygen, and ratiometric response gives these microparticles great potential as tools for quantitatively mapping the fluctuations in oxygen concentration that impact biological responses in cell and tissue engineering studies.

2. Materials and methods

All reagents were purchased from Fischer Scientific, Sigma-Aldrich, or otherwise noted.

2.1. Synthesis of fluorescent oxygen-sensing microparticles

A suspension of 2 g of silica gel (Davisil 710, 9.5-11 μm-diameter) and 40 mL of 0.01 N NaOH was stirred for 30 min. Next, 10 mL of a 0.5 mM solution (in ethanol) of the oxygen-sensitive luminophore tris (4,7-diphenyl-1,10-phenanthroline) ruthenium (II) dichloride, or $Ru(Ph_2phen_3)Cl_2$ (GFS Chemicals, Powell, OH), and 10 mL of a 0.5 mM solution (also in ethanol) of the oxygen-insensitive fluorophore Nile blue chloride, were added simultaneously. The mixture, deep green in color, was stirred for another 30 min. Next, the solution was centrifuged for 20 min at 1,900g and the supernatant was removed. The remaining particles were washed and centrifuged three times in 30 mL of deionized water and once in 30 mL of ethanol. After removal of the supernatant, the particles were dried at 70°C overnight.

A solution of 0.2 g of the dry luminophore-bound silica gel particles, 700 μL of hexane, 1 g of poly(dimethylsiloxane) (PDMS) pre-polymer, and 0.1 g of curing agent (Sylgard 184 elastomer kit; Dow Corning, Midland, MI) was vortexed for 1 min. A 2 w/v % solution of sodium dodecyl sulfate (SDS) in water (300 mL) was heated in a hot-plate to 70°C and magnetically stirred at 1,200 rpm using a 3.81-cm (1.5 inch) stir bar. The silica gel/PDMS solution was poured into the SDS solution and the resulting oil-in-water emulsion was heated and stirred for 7-8 h. Next, the emulsion was strained twice; first through a 0.5-mm sieve and then through a 25-mm sieve. The particles collected by the 25-mm sieve were washed and centrifuged three times in 30 mL of a 0.2 w/v % bovine serum albumin (BSA) in phosphate-buffered saline (PBS) solution with 0.1% methyl-4-hydroxybenzoate (methylparaben) for 20

min at 1,900g. After the final washing step, the particles were re-suspended to a density of ~50 particles/mL in 0.2% BSA in PBS and stored in the dark at 4°C.

2.2. Measurements of microparticle size distribution

Microparticle size distribution was measured using a Multisizer 3 Coulter counter (Beckman Coulter, Fullerton, California). Two batches of microparticles were combined and tested in three trials.

2.3. Cell culture and microparticle cytotoxicity

Microparticle cytotoxicity was assayed by comparing cell density during culture in the presence of the microparticles to that of the positive control (no particles). Mouse balb/3T3 fibroblasts (ATCC, Manassas, VA) were maintained in high glucose DMEM (Hyclone Laboratories, Logan, Utah) supplemented with 10% fetal bovine serum (FBS; Invitrogen, Carlsbad, CA), 40 mM L-glutamine (ATCC, Manassas, VA), and 50 μg/mL of penicillin/streptomycin (MP Biomedicals, Solon, OH). Fibroblasts were cultured in 24-well plates (Becton Dickinson, Franklin Lakes, NJ) at a density of 50,000 cells/well (25,000 cells/cm^2) for 24 and 48 h in the presence of 2,500 or 5,000 particles, which correspond to particle:cell ratios of 1:20 and 1:10, respectively. As a positive control, cells were also cultured under the same conditions without microparticles. The cells were fixed in 4% formaldehyde in PBS for 20 min. After fixation, cells were washed with PBS to remove the microparticles. Cell nuclei were stained with 300 nM 4,6-diamino-2-phenylindole (DAPI) in PBS for

10 min. After mounting with fluoromount-G (Southern Biotech, Birmingham, Al), fluorescence images of adherent cells were captured with an Olympus IX-81 (Olympus, Center Valley, PA) microscope. Image analysis was performed using NIH-ImageJ freeware.

2.4. Preparation of microparticle-embedded hydrogels

The poly(ethylene glycol) dimethacrylate (PEG-DM) was synthesized from 8000 Da poly(ethylene glycol). 10 g of PEG were dried of adsorbed water using azeotropic distillation in toluene (4 mL/g PEG), concentrated, and then dried overnight under vacuum. Under an argon purge, dry pyridine (3 mL/g PEG) was added to dissolve the PEG. This solution was cooled to 0°C in an ice bath. Methacrylic anhydride (4 molar excess to the moles of PEG) was added slowly with a syringe to PEG/pyridine solution still in the ice bath. The new solution was mixed in an ice bath for 10 min and then allowed to react for 48 h in the dark at room temperature. Working in minimal light, the reaction was diluted 10-15x with dichloromethane and washed twice with 1 M HCl to neutralize the reaction byproducts. The dichloromethane/PEG-DM solution was dried with sodium sulfate, filtered, concentrated to 50 mL, precipitated in ice-cold diethyl ether, filtered, and dried overnight under vacuum in the dark at room temperature. The desiccated PEG-DM product was stored at -20°C.

Percent methacrylation of PEG-DM was determined by ^{1}H-NMR (JEOL ECX 400MHz spectrometer) in deuterated dichloromethane: 1.9 (methacrylate CH_3), 3.4-3.6 (PEG), 4.2-4.3 (methacrylate CH_2), 5.5 and 6.0 (methacrylate CH on PEG-DM),

5.65 and 6.2 (unreacted methacrylic acid CH). Peak integration indicated that the degree of methacrylate substitution was 70% relative to the PEG terminal hydroxyl groups.

A clean glass slide was submerged in a solution of 200 mL of ethanol, 1 mL of 3-(trimethylsilyl)-propyl methacrylate, and 6 mL of 10% acetic acid for 3 min. The glass slide was then rinsed thoroughly with ethanol and air dried. Next, the glass slide was fitted with a casting mold consisting of a 0.5-mm thick silicone gasket (McMaster-Carr, Robbinsville, NJ) coated with vacuum grease. The PEG-DM was crosslinked and covalently bound to the methacrylate-modified glass slide in a free-radical crosslinking reaction: first, 0.015 g of PEG-DM and 1.5 μL of N,N,N',N'-tetra-methylethylene-diamine (TEMED) were added to 150 μL of the 0.2 w/v % BSA/PBS solution containing 54 ± 10 particles/μL (measured value). Second, 7.5 μL of 20 w/v % ammonium persulfate (APS) in PBS solution were added to the PEG-DM monomer solution. Finally, the solutions were vortexed, immediately transferred to the glass slide mold, and allowed to react overnight. The construct was stored in water at 4°C until use. Average gel thickness after crosslinking was 250 μm.

Confocal laser microscopy was also employed to image the sensing microparticles inside the PEG-DM hydrogel. Images were taken with a Leica TCS SP5 confocal microscope (Leica Microsystems, Bannockburn, IL) in 5-μm steps from the top to the bottom of the samples. Stacks were reconstructed to create a 3D image of the sensing microparticles throughout the PEG-DM hydrogel using the computer software Volocity (Improvision, Waltham, MA).

2.5. Parallel-plate flow chamber system

The microparticle-embedded PEG-DM hydrogels were placed into a parallel-plate flow chamber and applied to calibrate microparticle fluorescence to dissolved oxygen content and determine sensor reversibility. The flow chamber (adapted from Munn et al. [79]), consisted of three sections that were held together by vacuum: (1) a polycarbonate block that served as the top section of the flow area, (2) a 1-mm thick silicone gasket (McMaster-Carr), which determined the total height of the flow area, and (3) a glass slide that served as the bottom of the flow chamber and held the hydrogel sample containing the sensing microparticles. The flow chamber was mounted on the stage of the fluorescence microscope and was connected in circuit form to a 500-mL water reservoir and a peristaltic pump via 1.6-mm ID/4.8-mm OD Tygon tubing (Cole-Parmer, Vernon Hills, IL). Water flow rate through flow chamber system was set at 5 mL/min. The water reservoir housed a traditional dissolved oxygen meter (VWR, West Chester, PA) and was also connected to two rotameters (Cole-Parmer, Vernon Hills, IL) that were used to control incoming gas flow from a nitrogen tank and a small air pump to the reservoir.

2.6. Microparticle calibration

To obtain microparticle fluorescence intensity data as a function of dissolved oxygen content, nitrogen and air were combined to achieve step-wise increments in dissolved oxygen concentration in the flow chamber water reservoir. The reservoir was initially sparged with nitrogen to remove dissolved oxygen from the water. Gas mixture percentages used were 100/0, 94/6, 85/15, 70/30, 60/40, 40/60, 30/70, and

0/100 (vol. % nitrogen)/(vol. % air). Each step change in gas mixture was made after the dissolved oxygen meter indicated that the dissolved oxygen in the reservoir had stabilized. The time elapsed between each step change was 10 min. Oxygen readings from the dissolved oxygen meter and fluorescent images of the sensing microparticles were recorded every 30 s. Each image was captured using a QDOT-605 filter set (Olympus, Center Valley, PA) for $Ru(Ph_2phen_3)Cl_2$ and a Cy5 filter set (Olympus) for Nile blue chloride. Excitation and emission wavelengths for $Ru(Ph_2phen_3)Cl_2$ are 470 and 610 nm, respectively, and Nile blue chloride are 636 and 656 nm, respectively. Exposure times for both $Ru(Ph_2phen_3)Cl_2$ and Nile blue chloride were 100 ms.

Image analysis was conducted using NIH Image-J freeware. Using line profiles (or line scans) across the width of a particular image (at 4x magnification, image area was 2.218 x 1.651 mm), average values of microparticle fluorescence intensity across the surface of the hydrogel were obtained. Each image was segmented with a series of line profiles from which an average value of intensity was determined. Images displaying $Ru(Ph_2phen_3)Cl_2$ and Nile blue chloride fluorescence were analyzed separately. Therefore, non-fluorescent particles were omitted from the analysis. Although the image analysis performed for the calibration and reversibility experiments was a global measurement of fluorescence intensity across the image area, individual particle analysis may also be performed. Additionally, the analysis may be optimized depending on the application and/or microparticle distribution and concentration in the sample.

To calibrate microparticle fluorescence to dissolved oxygen content, two models were explored. First, we adapted a conventional Stern-Volmer model that

describes the relationship between fluorescence intensity of the $Ru(Ph_2phen_3)Cl_2$ luminophore and oxygen concentration and normalizes the fluorescence intensity of $Ru(Ph_2phen_3)Cl_2$ with the Nile blue chloride reference fluorophore:

$$\frac{I_{R,0}}{I_R} - 1 = K_{SV}[O_2] \tag{3}$$

where $I_{R,0}$ and I_R are the ratios of the fluorescence intensities of $Ru(Ph_2phen_3)Cl_2$ and Nile blue chloride in the absence and presence of oxygen respectively, K_{SV} is the Stern-Volmer quenching constant, and $[O_2]$ is the concentration of oxygen. Second, we also applied a two-site Stern-Volmer model:

$$\frac{I_{R,0}}{I_R} = \left(\frac{f_1}{1 + K_{SV,1}[O_2]} + \frac{f_2}{1 + K_{SV,2}[O_2]}\right)^{-1} \tag{4}$$

This model, proposed by Carraway et al. [58], states that the oxygen-sensitive luminophore is distributed mainly in two populations through the matrix of a polymer, a quenched population and an unquenched population (with fractions f_1 and f_2 respectively), each with its own quenching constant ($K_{SV,1}$ and $K_{SV,2}$). The quenching constant for the unquenched population ($K_{SV,2}$) is very small and is generally assumed to be negligible. Thus, with this assumption (and the fact that $f_2 = 1 - f_1$), Equation 4 can then be rearranged to:

$$\frac{I_{R,0} - I_R}{I_{R,0}(f_1 - 1) + I_R} = K_{SV}[O_2] \tag{5}$$

resulting in a simpler two parameter fit (i.e., f_1 and K_{SV}).

2.7. Microparticle reversibility

Characterization of microparticle reversibility was carried out in a similar fashion as for the calibration. However, only changes from 100% nitrogen to 100% air were employed. As with the microparticle calibration, the changes in dissolved oxygen concentration were made after measured dissolved oxygen inside the flow chamber water reservoir was observed to remain stable. The time elapsed between each change was 12.5 min. Oxygen readings from the dissolved oxygen meter and fluorescent images of the sensing microparticles were recorded every 30 s. System equilibration time, which accounts for time required for oxygen saturation in the water reservoir as well as the sensor response time, was evaluated as the time elapsed to obtain 90% of the stabilized sensor response after a change from 100% nitrogen to 100% air was effected.

2.8. Statistical analysis

Statistical analysis for microparticle cytotoxicity and reversibility experiments was performed using ANOVA with a cutoff of $p < 0.05$. Statistical analysis for system equilibration times as measured by the microparticles and traditional dissolved oxygen meter was performed using a Student's t-test with a cutoff of $p < 0.05$.

3. Results

3.1. Microparticle synthesis and size distribution

Synthesis of the fluorescent oxygen-sensing microparticles consisted of two steps: (1) immobilization of the oxygen-sensitive luminophore $Ru(Ph_2phen_3)Cl_2$ and the oxygen-insensitive fluorophore Nile blue chloride to silica gel and (2) the encapsulation of the luminophore-bound silica gel with PDMS via an oil-in-water emulsion. Fluorescent images were captured with a fluorescence microscope after curing of the PDMS. Subsequently, images of the sensing microparticles inside the PEG-DM hydrogel samples were also taken with a confocal microscope. Imaging results are shown in Figure 3. Figure 3a shows a fluorescence image of the sensing microparticles, where the red fluorescence marks the $Ru(Ph_2phen_3)Cl_2$ luminophore and the blue pseudo-color marks the Nile blue chloride. Figure 3b shows the same fluorescent image with a phase contrast image overlaid. Figure 3c displays a 3D reconstruction of the sensing microparticles suspended through the matrix of the hydrogel sample. Confocal z-stacks were also converted to movies that depict the 3D distribution and resolution of the microparticles.

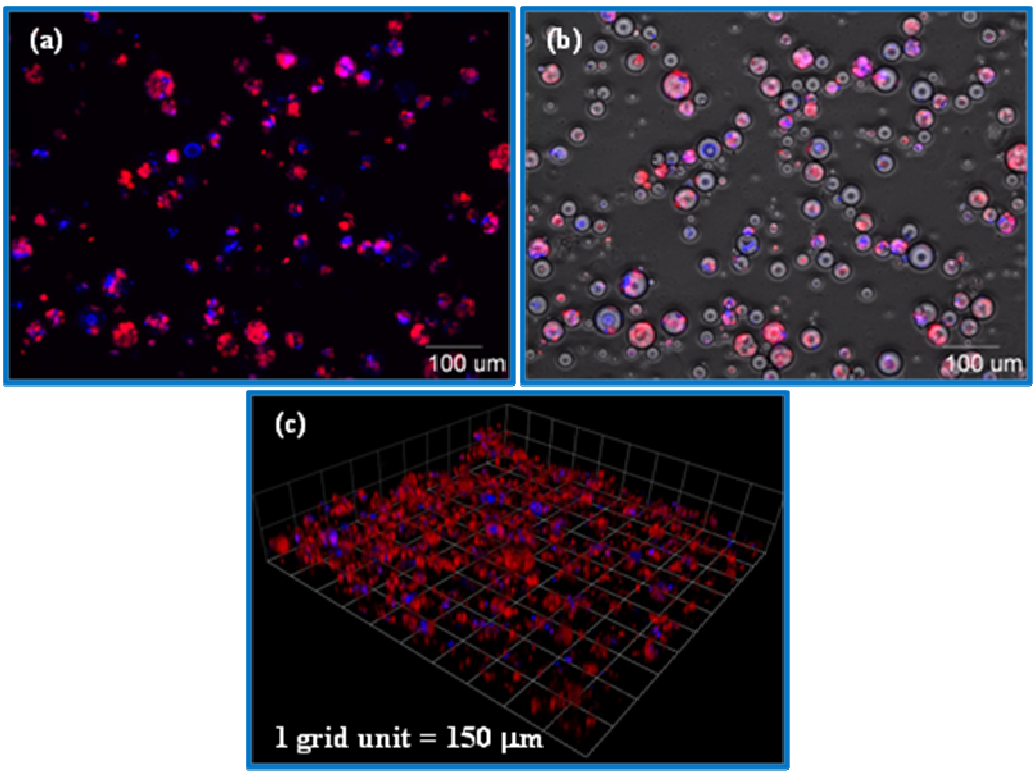

Figure 3: Images of oxygen-sensing microparticles captured after curing of PDMS. **(a)** Red fluorescence marks the oxygen-sensitive luminophore $Ru(Ph_2phen_3)Cl_2$ and blue pseudocolor marks the reference fluorophore Nile blue chloride. **(b)** Fluorescent image of sensing microparticles with phase contrast image overlaid. **(c)** Confocal image of sensing microparticles distributed throughout matrix of PEG-DM hydrogel sample (1 grid unit = 150 µm).

Microparticle size distribution was measured for two combined batches of particles. As shown in Figure 4, the emulsion process yields fluorescent microparticles wherein 70% of their size distribution falls in the 5-40 µm range.

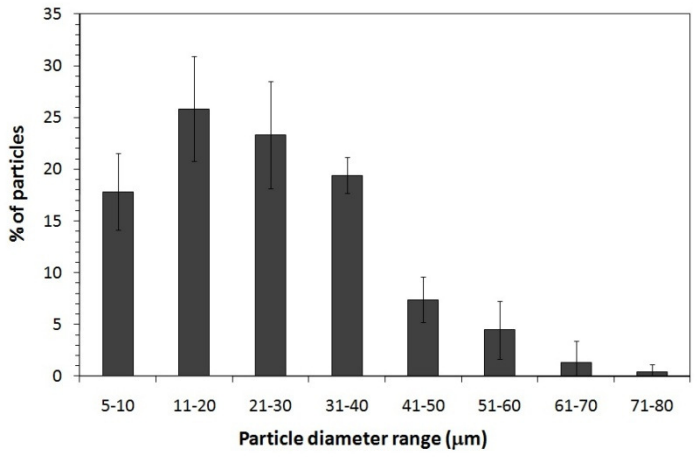

Figure 4: Size distribution for oxygen-sensing microparticles as measured with a Coulter counter. Data shown as mean ± standard error for two batches combined and tested in three trials.

3.2. Microparticle cytotoxicity

To assay microparticle toxicity, balb/3T3 fibroblasts were cultured for up to 48 h in the presence of the oxygen-sensing microparticles. Cell densities in treated and untreated (positive control) samples were based on counts of the DAPI-stained cell nuclei of adherent cells. Figure 5 shows cell densities at 24 and 48 h for cells cultured at particle:cell ratios of 1:10 and 1:20 (the particle:cell ratios were selected based on preliminary studies in two- and three-dimensional systems to probe oxygen content in the local cellular microenvironment). Statistical analysis performed using ANOVA ($p < 0.05$) demonstrated that the cell densities of the treated and untreated wells were not statistically different, affirming that the microparticles are not cytotoxic to the cells under standard cell culture conditions for up to 48 h.

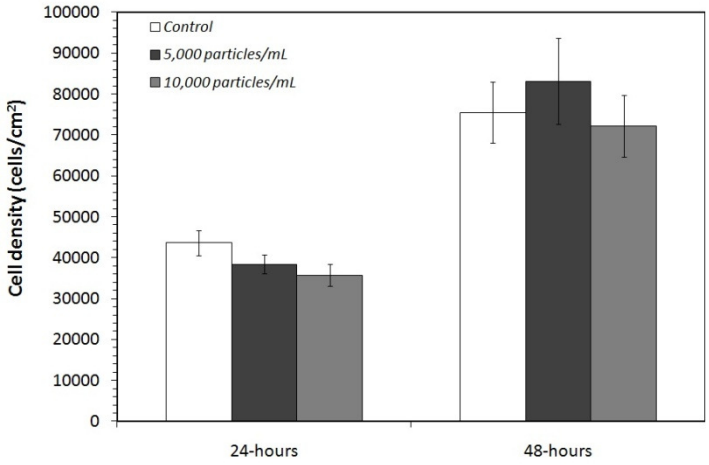

Figure 5: Cell densities (in cells/cm^2) at 24 and 48 h for Balb/3T3 mouse fibroblasts cultured in the presence of two oxygen-sensing microparticle densities representative of particle:cell ratios useful for probing cell microenvironment in two- and three-dimensional studies. ANOVA analysis indicated that there is no statistical difference between treatments at each time point, signifying that the microparticles are non-cytotoxic to the cells under standard in vitro conditions. Data shown as mean ± standard error for six trials.

3.3. Microparticle calibration

The calibration of microparticle response when suspended in a three-dimensional hydrogel was performed in a flow chamber such that the oxygen content of the aqueous environment of the hydrogel could be systematically controlled. Nitrogen and air were combined and sparged into the water reservoir to achieve step-wise increments in the aqueous dissolved oxygen concentration. Oxygen concentration inside the water reservoir was monitored with a traditional dissolved oxygen meter. Change in microparticle fluorescence intensity to the changes in oxygen concentration in the water was monitored by capturing fluorescent images of the sensing microparticles with the fluorescence microscope.

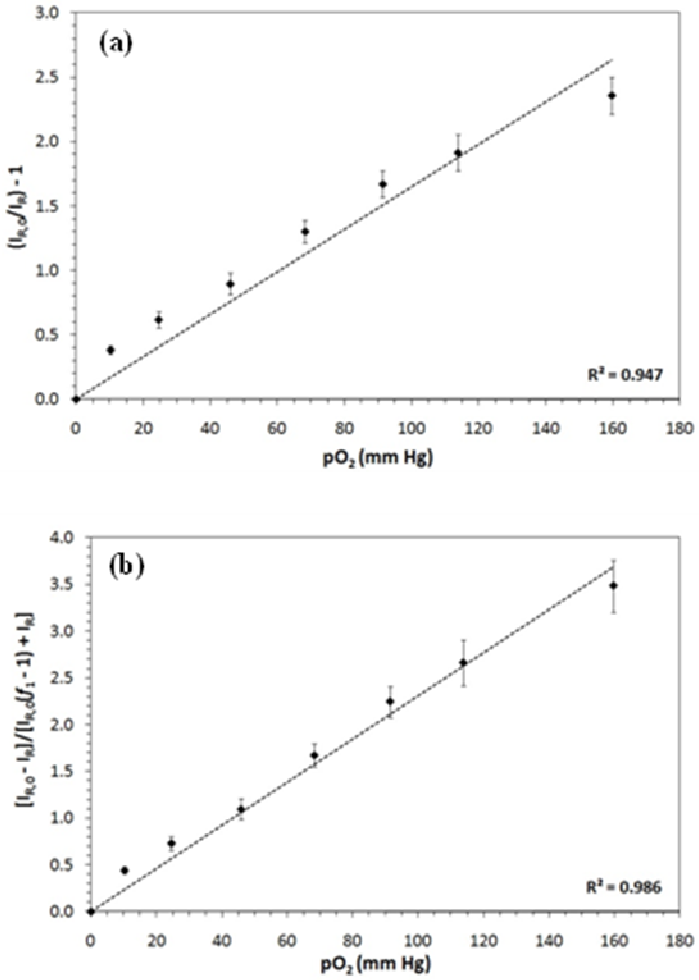

Figure 6: Calibration of oxygen-sensing microparticles using the conventional Stern-Volmer model (**a**; R^2 = 0.947) and the two-site Stern-Volmer model (**b**; R^2 = 0.986). Data points in each plot are shown as mean ± standard error of normalized intensity data obtained from three calibrations performed on microparticles at the surface of a three-dimensional PEG-DM hydrogel sample. Model fits are represented by dashed lines.

To correlate fluorescence intensities to dissolved oxygen content, we explored two models to fit data for the sensing microparticles in the range of 0-160 mm Hg, or 0 to 100% oxygen saturation of the water. Figure 6a shows the conventional Stern-

Volmer calibration (based on Equation 3). Regression results were 0.017 for the Stern-Volmer quenching constant (K_{SV}, mm Hg^{-1}) and $R^2 = 0.947$. Figure 6b shows the calibration of the sensing microparticles using the two-site Stern-Volmer equation (based on Equation 5). Regression results for the two-site Stern-Volmer model were 0.023 mm Hg^{-1} for K_{SV} and $R^2 = 0.986$. The value obtained for the quenched fluorophore fraction (f_1) was 0.90 ± 0.02.

Figure 6 demonstrates that the sensing microparticles are capable of measuring dissolved oxygen concentrations (partial pressures) in ranges relevant to tissue culture studies; mainly, < 20 mm Hg (hypoxic conditions), 30-90 mm Hg (normoxic conditions), and 100-150 mm Hg (hyperoxic conditions).

3.4. Microparticle reversibility

To test microparticle reversibility, nitrogen and air were alternated during the course of the experiment. As with calibration, oxygen concentration inside the water reservoir was monitored using the dissolved oxygen meter. Changes in microparticle fluorescence were monitored by capturing images with the fluorescence microscope. These two operations were also carried out simultaneously. Gas content was switched only after the reading from the dissolved oxygen meter had stabilized. Figure 7a shows microparticle reversibility compared to that of the traditional dissolved oxygen meter. Both the dissolved oxygen meter and the sensing microparticles demonstrated good recovery while the environment was alternated between oxygenated and deoxygenated water. No evidence of hysteresis was observed. Figure 7b shows the minimum and maximum response (for 100% air and 100% nitrogen respectively) of

the oxygen-sensing microparticles. Statistical analysis performed using ANOVA ($p < 0.05$) demonstrated that there is no difference within sets of intensity minima and maxima.

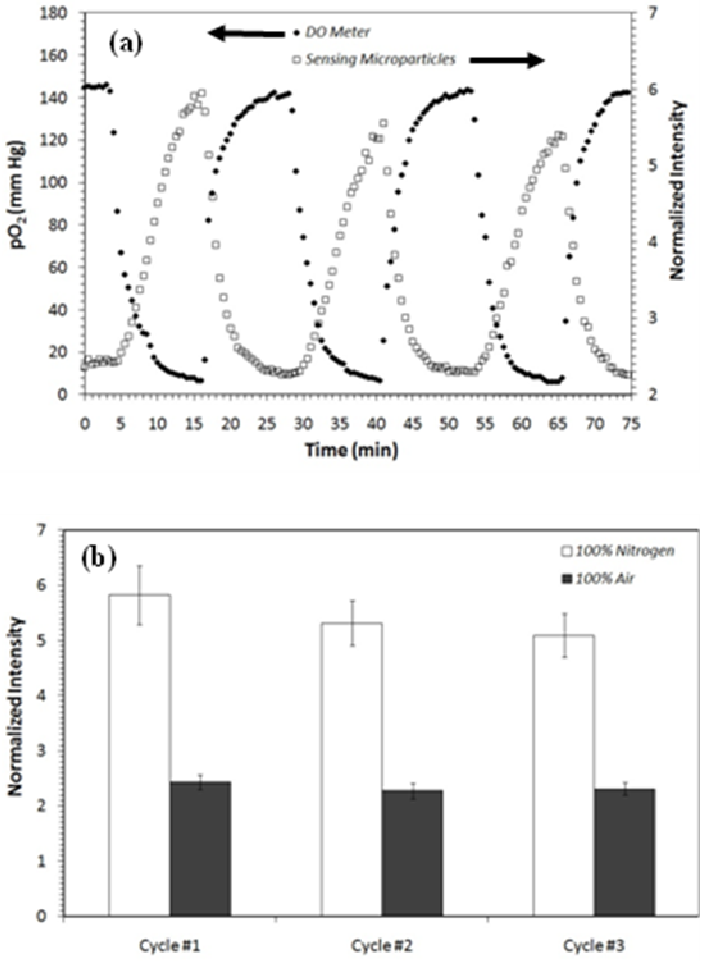

Figure 7: (a) Typical reversibility response of oxygen-sensing microparticles compared to that of traditional dissolved oxygen meter. Arrows displayed on plot legend point to respective axes; left axis for dissolved oxygen meter data and right axis for microparticle data. **(b)** Normalized intensity values of oxygen-sensing microparticles for high and low oxygen content (water reservoir sparge of 100% air and 100% nitrogen respectively) during reversibility experiments. ANOVA analysis indicated that there is no statistical difference between the sets of intensity minima and maxima measured at both conditions. Data shown as mean ± standard error for three trials.

System equilibration times as measured by the dissolved oxygen meter and sensing microparticles were (mean ± standard error) 5.2 ± 1.0 and 5.6 ± 0.4 min, respectively. Student's t-test ($p < 0.05$), demonstrated that the two calculated values of equilibration time were not different.

4. Discussion

To design the microparticle sensors, $Ru(Ph_2phen_3)Cl_2$ was chosen because of its high quantum yield, high oxygen quenching, and thermal stability at physiological temperature [57, 80]. Synthesis of the sensing microparticles is a simple and inexpensive two-step process. The first step consisted of immobilization of $Ru(Ph_2phen_3)Cl_2$ and Nile blue chloride, to silica gel particles 9.5-11 μm in diameter. The reference fluorophore, Nile blue chloride, allows ratiometric (or normalized) measurements that correct for the typical drawbacks of fluorescence intensity measurements such as bleaching, heterogeneous fluorophore concentration, fluctuations in excitation light intensity, and camera sensitivity. The immobilization process was adapted from John et al. [61], who immobilized $Ru(Ph_2phen_3)Cl_2$ and the reference fluorophore safranin onto silica gel. In contrast, we used Nile blue chloride as our reference fluorophore due to the fact that safranin's emission spectrum overlaps with that of $Ru(Ph_2phen_3)Cl_2$. The differing emission spectra between the $Ru(Ph_2phen_3)Cl_2$ and the Nile blue chloride allowed us to identify and independently measure their fluorescence inside the microparticles with the fluorescence microscope. Conversely, the absorption spectrum of Nile blue chloride was found to

overlap with the emission spectrum of $Ru(Ph_2phen_3)Cl_2$, which might lead to fluorescence resonance energy transfer (FRET) between the two fluorophores. Thus, negligible FRET was a key criterion in the development of the reported microparticle synthesis procedure. The absence of FRET was confirmed in gas phase experiments using PDMS films containing silica gel bound with $Ru(Ph_2phen_3)Cl_2$ and Nile blue chloride (data not shown).

The second microparticle synthesis step consisted of the encapsulation of the modified silica gel within PDMS. PDMS is optically transparent, hydrophobic, non-cytotoxic, and highly permeable to gases such as oxygen, nitrogen, and carbon dioxide [81]. For instance, the diffusivity of oxygen in PDMS is approximately twice that of oxygen in water (4.1×10^{-5} cm^2/s and 2.1×10^{-5} cm^2/s for PDMS and water respectively at room temperature) [82]. Therefore, by encapsulating the $Ru(Ph_2phen_3)Cl_2$- and Nile blue chloride-modified silica gel within PDMS, we ensure relatively unrestricted oxygen transport from the culture medium to the luminophore. Moreover, preliminary cell culture studies indicated that cell viability was not adversely affected by the presence of the microparticles in the cell microenvironment (Figure 5), which suggests that encapsulation in PDMS also provides a protective barrier to inhibit luminophore leaching into the cell culture environment.

The emulsion process yielded microparticles that were predominantly in the 5-40 μm range (Figure 4). This size range is optimal for the sensing microparticles, as it is on the size range of cells, yet large enough to prevent endocytosis. Furthermore, this small size range minimizes diffusion limitations of oxygen from the medium to the luminophore and significantly reduces sensor response time [64, 83]. Due to the

wide size range of the microparticles, heterogeneity in their distribution through the hydrogel volume was expected. We compensated for this effect by using high particle concentrations (54 ± 10 particles/μL) in the PEG-DM hydrogels.

Microparticle calibration inside a three-dimensional hydrogel and characterization of the microparticle reversibility were carried out using a parallel-plate flow chamber mounted on a fluorescence microscope stage. In addition, to demonstrate the functionality of the sensing microparticles, their reversibility was compared to that of a traditional dissolved oxygen meter. The flow chamber system allowed for systematic control of the dissolved oxygen in the microparticle environment as well as simultaneous measurements of oxygen concentration and changes in microparticle fluorescence intensity. The oxygen concentration of the inlet solution was monitored with a dissolved oxygen meter while the response of the microparticle sensors was monitored via fluorescence images captured at the midpoint of the flow chamber length.

Retaining the reversibility of the $Ru(Ph_2phen_3)Cl_2$ luminophore after the immobilization and encapsulation steps is important for sensor operation in environments with fluctuating oxygen concentration. As shown in Figures 7a and 7b, both the dissolved oxygen meter and the microparticle sensors demonstrated good recovery. Statistical analysis demonstrated that there is no difference within sets of normalized intensity minima and maxima. No evidence of hysteresis was observed, as both responses were capable of returning to their initial state between cycles. Also, using both the microparticles, as well as the traditional dissolved oxygen probe, we determined the time for system equilibration, which accounts for the time required for

oxygen saturation in the water reservoir as well as the sensor response time. The system equilibration times are equal, suggesting that the response time of both sensors in the flow-loop apparatus is limited by the rate of oxygen transport through water rather than sensor performance.

Calibration of microparticle fluorescence intensity to dissolved oxygen content (Figure 6) demonstrates that the microparticle sensors were capable of measuring oxygen partial pressures in ranges relevant to tissue culture studies. It is interesting to note that the conventional Stern-Volmer model (Equation 3), which pertains to luminophore in solution, predicts a linear response of the $Ru(Ph_2phen_3)Cl_2$ luminophore to oxygen. However, when the luminophore is embedded in a polymeric support, its response ceases to be linear (Figure 6a). The demonstrated downward curvature is expected due to heterogeneities in the polymer structure and non-uniform distribution of luminophore molecules throughout a polymer matrix [56, 58, 80]. Hence, the two-site model of the Stern-Volmer equation (Equation 5) was also applied.

As demonstrated by the regression results (Figure 6b), the two-site Stern-Volmer equation is a better fit for the calibration data than the conventional Stern-Volmer model. The value obtained for the quenched luminophore fraction (f_1) was 0.90 ± 0.02. Reported values for f_1 have ranged from 0.97 for the $Ru(Ph_2phen_3)Cl_2$ luminophore in PDMS films [58], to 0.73 in poly(styrene) films [84], and to 0.61 while adsorbed on mesoporous silica particles suspended in self-assembled polymer films [85]. The value obtained from our experiments is closer to that obtained by Carraway et al. [58], which pertains to $Ru(Ph_2phen_3)Cl_2$ in PDMS. Our result reflects

that approximately 90% of the available oxygen-sensitive luminophore is quenched under our particular testing conditions. The differences observed in the reported values of f_1 suggest that this value is mainly dependent on the material contacting the luminophore. For example, the polarity of the environment in which the $Ru(Ph_2phen_3)Cl_2$ luminophore is present affects fluorescence quenching by oxygen. Xu et al. [56] demonstrated that when the $Ru(Ph_2phen_3)Cl_2$ luminophore was immobilized onto a polar carrier, such as silica, and added to a non-polar silicone polymer material, fluorescence quenching by oxygen was enhanced. They speculated that the luminophore was partitioned between two fractions, one present in the polar silica and one preset in the non-polar silicone polymer, resulting in decreased fluorescence quenching by oxygen and a downward curvature observed in the Stern-Volmer plot. This partition was due to the low solubility of the luminophore in the non-polar polymer. Therefore, one possible explanation for the value we have obtained for quenched luminophore fraction (f_1) is that it corresponds to a fraction of luminophore that exists immobilized onto the silica gel (90%); whereas, the remaining fraction (10%) exists, or is in contact with, the PDMS. This partition decreases fluorescence quenching by oxygen of the luminophore and deviates the Stern-Volmer calibration of the sensing microparticles from linearity. These results demonstrate that the silica/PDMS system we have employed was a suitable choice for our design. Moreover, PDMS is non-cytotoxic, transparent, and easy to process; thus, the reported oxygen-sensing microparticle system presents significant advantages in terms of performance as well as ease of manufacturing and application in cell culture studies using a readily adaptable fluorescence microscopy analysis.

5. Conclusions

Here, we have described the development and characterization of fluorescent oxygen-sensing microparticles. We have demonstrated that the luminophore-bound microparticles can be suspended in a transparent biomaterial and can be used to obtain ratiometric measurements of temporal changes in oxygen concentrations by monitoring fluorescence intensity with a fluorescence microscope. Synthesis of the microparticles is a simple two-step process, which yielded microparticles in a size distribution predominantly in the 5-40 μm range. The microparticles were demonstrated to be non-cytotoxic to cells during culture. Sensing microparticle response showed good reversibility and no evidence of hysteresis was observed. Additionally, the measured system equilibration time was comparable to that of a traditional dissolved oxygen meter and calibration demonstrated that the sensors were capable of measuring oxygen partial pressures in ranges relevant to tissues culture studies. While the conventional Stern-Volmer model showed acceptable results for fitting the microparticle calibration data, the two-site Stern-Volmer model resulted in the best fitting results and the calculated fraction of quenched $Ru(Ph_2phen_3)Cl_2$ for the sensing microparticles was close to that reported in literature for the same luminophore in PDMS.

CHAPTER 3: Fluorescent silica particles for monitoring oxygen levels in three-dimensional cellular structures

1. Introduction

Staphylococcus aureus is a bacterial pathogen that has been associated with hospital-acquired infections, such as those related to prosthetic device implantations [16]. *S. aureus* infections have proven difficult to treat due to their ability to form organized biofilms [17], which contribute to antibiotic resistances [18, 19] and secondary metastatic infections caused by free flowing planktonic-cells that detach from the biofilms [20]. Whereas the effects of soluble factors on planktonic cell adhesion and biofilm formation have been investigated [21], much is still unknown about processes that are unique to the biofilm interior, such as oxygen transport dynamics, that may contribute to antibiotic resistance and the formation of secondary infections. This is due to the lack of adequate tools to map oxygen transport through biofilms.

Optical oxygen sensors based on fluorescence quenching have shown great potential for quantitatively mapping oxygen concentration in cell culture studies. Various sensors of this type have been developed using a wide variety of formats, such as patches [60], sensor films [61], fiber optics [63, 65], and nanoprobes [59, 87]. Recently, we reported fluorescent oxygen-sensing particles which can be suspended within any transparent biomaterial and utilized to measure temporal and spatial changes in oxygen concentration through the volume of a biomaterial (Chapters 2 [88]). Herein, we report an adaptation of this technology for the development of

fluorescent microparticles suitable to measure oxygen profiles within bacterial biofilms. The particles were synthesized using two adaptations of the Stöber method for hydrolysis of tetraethylorthosilicate (TEOS) [71, 74, 89] that yielded particles roughly the size of *S. aureus* cells (~1 μm). One protocol regarded the synthesis of the particles, followed by the immobilization of an oxygen-sensitive fluorophore and a reference fluorophore to their surface. The second protocol regarded the encapsulation of the two fluorophores within the particles during synthesis. Use of the Stöber synthesis has been reported previously for other optical sensing applications, such as for the detection of nitro compounds like trinitrotoluene (TNT) [75]. We present the characterization of the properties of the microparticles yielded by the two synthesis protocols, as well as a comparison of these properties between the two. Additionally, we demonstrate that the microparticles are suited for studies of oxygen transport within *S. aureus* biofilms by performing simultaneous culture of a biofilm within a biomaterial substrate with the microparticles suspended through its volume.

2. Materials and methods

All reagents were purchased from either Fisher Scientific or Sigma-Aldrich unless otherwise noted.

2.1. Synthesis of fluorescent silica microparticles

The oxygen-sensing particles were synthesized by adapting the Stöber method [66] to allow for immobilization of fluorophores onto the silica particles. Two protocols were used. For the first protocol (dye-coated microparticles), three solutions were prepared. Solution A: 4 mL of 30% ammonium hydroxide, 3.5 mL of water, 17.5 mL of 1:3 (v:v) methanol-propanol solution. Solution B: 4 mL 1:3 methanol-propanol, 1 mL of TEOS. Solution C: 32 mL of 1:3 methanol-propanol and 8 mL of TEOS. Solutions A and B were combined in a flask suspended in a 25°C bath and stirred for 15 min. Then solution C was added drop-wise and stirred for 4 hrs. The solution was centrifuged (1900g) for 10 min and the particles were resuspended in deionized water; this washing procedure was carried out four times with deionized water and once with ethanol. The particles were then dried overnight at 70°C. Next, two fluorophores were immobilized onto dry particles, the oxygen-sensitive fluorophore tris (4,7-diphenyl-1,10-phenanthroline) ruthenium (II) dichloride, or $Ru(Ph_2phen_3)Cl_2$, and the oxygen-insensitive fluorophore Nile blue chloride. A suspension of 2 g of the silica particles and 40 mL of 0.01 N NaOH was stirred for 30 min. Next, 10 mL of a 0.5 mM solution of $Ru(Ph_2phen_3)Cl_2$ (GFS Chemicals, Powell, OH) in ethanol, and 10 mL of a 0.5 mM solution of Nile blue chloride in ethanol, were added simultaneously and stirred for 30 min. The particles were then washed and dried as above and stored in the dark.

The second protocol (dye-encapsulated microparticles) involved the encapsulation of the fluorophores within the silica particles by their addition to the catalyst solution during synthesis. Two solutions were prepared. Solution A: 4 mL of

30% ammonium hydroxide, 3.5 mL of water, 17.5 mL of ethanol, 3 mg of $Ru(Ph_2phen_3)Cl_2$, and 1 mg of Nile blue chloride. Solution B: 4 mL ethanol and 1 mL of TEOS. Solutions A and B were combined in a flask suspended in a 25°C bath and allowed to react for 3 hrs. The solution was centrifuged (1900g) for 10 min and the particles were resuspended in deionized water; the washing procedure was repeated up to 7 times or until the supernatant was observed clear. The remaining particles were then lyophilized overnight, until a fine powder was obtained.

After synthesis, the microparticles were imaged using a JEOL JSM-5600 Scanning Electron Microscope (JEOL, Tokyo, Japan) to assess their size and morphology. Sputter coating on the microparticles for microcopy was performed with a Denton Vacuum Desk II (Denton Vacuum, Moorestown, New Jersey) at 45 A for 60 seconds.

2.2. Preparation of microparticle embedded PEG-DM hydrogels

The poly(ethylene glycol) dimethacrylate was synthesized as described in Chapter 2, Section 2.2. To prepare the PEG-DM hydrogels utilized for calibration of the particles, a clean glass slide was submerged in a solution of 200 mL of ethanol, 1 mL of 3-(trimethylsilyl)-propyl methacrylate, and 6 mL of 10% acetic acid for 3 min. The glass slide was then rinsed thoroughly with ethanol and air dried. Next, the glass slide was fitted with a casting mold consisting of a 0.5-mm thick silicone gasket (McMaster-Carr, Robbinsville, NJ) coated with vacuum grease. The PEG-DM was crosslinked and covalently bound to the methacrylate-modified glass slide in a free-radical crosslinking reaction. First, 0.015 g of PEG-DM, 5 mg of the fluorescent silica

particles, and 1.5 μL of N,N,N',N'-tetra-methylethylene-diamine (TEMED) were added to 150 μL of 0.2 w/v % BSA/PBS solution. The solution was sonicated for 5 minutes, to break particle clumps, and vortexed thoroughly. Second, 7.5 μL of 20 w/v % ammonium persulfate (APS) in PBS solution were added to the PEG-DM monomer solution. Finally, the solutions were vortexed, immediately transferred to the glass slide mold, and allowed to react for 3 hours. Two gels were prepared, one for each type of particles. The constructs were stored in water at room temperature and in the dark until use.

2.3. Parallel-plate flow chamber system

The microparticle-embedded PEG-DM hydrogels were placed into a parallel-plate flow chamber and applied to calibrate microparticle fluorescence to dissolved oxygen content. The flow chamber (adapted from Munn et al. [79]), consisted of three sections that were held together by vacuum: (1) a polycarbonate block that served as the top section of the flow area, (2) a 1-mm thick silicone gasket (McMaster-Carr), which determined the total height of the flow area, and (3) a glass slide that served as the bottom of the flow chamber and held the hydrogel sample containing the sensing microparticles. The flow chamber was mounted on the stage of the fluorescence microscope and was connected in circuit form to a 500-mL water reservoir and a peristaltic pump via 1.6-mm ID/4.8-mm OD Tygon tubing (Cole-Parmer, Vernon Hills, IL). Water flow rate through flow chamber system was set at 5 mL/min. The water reservoir housed a traditional dissolved oxygen meter (VWR, West Chester, PA) and was also connected to two rotameters (Cole-Parmer, Vernon Hills, IL) that

were used to control incoming gas flow from a nitrogen tank and an air tank to the reservoir.

2.4. Microparticle calibration

Microparticle fluorescence intensity data as a function of dissolved oxygen content was obtained by combining nitrogen and air to achieve step-wise increments in dissolved oxygen concentration in the water reservoir. The reservoir was initially sparged with nitrogen to remove dissolved oxygen from the water. The gas mixture percentages used were 100/0, 94/6, 85/15, 70/30, 60/40, 40/60, 30/70, and 0/100 vol. % nitrogen/vol. % air. Each step change in gas mixture was effected after dissolved oxygen in the water reservoir was observed to stabilize, as indicated by the dissolved oxygen meter. The time elapsed between each step change was 10 min. Oxygen readings from the dissolved oxygen meter and fluorescence images of the sensing microparticles were recorded every 30 s. Each image was captured using a QDOT-605 filter set (Olympus, Center Valley, PA) for $Ru(Ph_2phen_3)Cl_2$ and a Cy5 filter set (Olympus) for Nile blue chloride. Excitation and emission wavelengths for $Ru(Ph_2phen_3)Cl_2$ are 470 and 610 nm, respectively, and Nile blue chloride are 636 and 656 nm, respectively. Exposure times for $Ru(Ph_2phen_3)Cl_2$ and Nile blue chloride were 100 and 1000 ms respectively.

Image analysis was conducted using NIH Image-J freeware. Mean values of microparticle fluorescence intensity across the surface of the hydrogel were obtained by using a series of line profiles to segment by each image across their width (at 4x magnification, image area was 2.218 x 1.651 mm). Images displaying

$Ru(Ph_2phen_3)Cl_2$ and Nile blue chloride luminescence were analyzed separately, excluding non-luminescent microparticles from the analysis.

To calibrate microparticle fluorescence to dissolved oxygen content, we adapted the conventional Stern-Volmer model to describe the relationship between fluorescence intensity of the $Ru(Ph_2phen_3)Cl_2$ luminophore and oxygen concentration and normalize its fluorescence intensity to that of the Nile blue chloride reference fluorophore:

$$\frac{I_{R,0}}{I_R} - 1 = K_{SV}[O_2] \tag{3}$$

where $I_{R,0}$ and I_R are the ratios of the fluorescence intensity of $Ru(Ph_2phen_3)Cl_2$ and Nile blue chloride in the absence and presence of oxygen respectively, K_{SV} is the Stern-Volmer constant, and $[O_2]$ is the oxygen concentration. However, Carraway et al. demonstrated that for luminescent organic-metal complexes immobilized on a polar carrier, such as $Ru(Ph_2phen_3)Cl_2$ immobilized on silica, a two-site Stern-Volmer model is better suited for calibration [58].

$$\frac{I_{R,0}}{I_R} = \left(\frac{f_1}{1 + K_{SV,1}[O_2]} + \frac{f_2}{1 + K_{SV,2}[O_2]} \right)^{-1} \tag{4}$$

The two-site Stern-Volmer model states that the $Ru(Ph_2phen_3)Cl_2$ luminophore is divided into two populations through the volume of the non-polar matrix, a quenched population and an unquenched population, with fractions f_1 and f_2 and their own

quenching constants $K_{SV,1}$ and $K_{SV,2}$ respectively. Two assumptions were applied to equation 2 for simplification: (1) $f_2 = 1 - f_1$ and (2) the quenching constant for the unquenched ($K_{SV,2}$) populations is very small and can be assumed to be negligible. Now we can rearrange equation 2 to have the form:

$$\frac{I_{R,0} - I_R}{I_{R,0}(f_1 - 1) + I_R} = K_{SV}[O_2] \tag{5}$$

which results in a simpler two-parameter fit.

2.5. Preparation of microparticle embedded collagen coated cover slips

First, 136.2 µL of type I rat tail collage (BD Biosciences, Bedford, MA) were mixed with 25 µL of 10x Hanks buffer and 3.0 µL of 1 M NaOH. An additional 0.1 µL of 1 M NaOH was used to adjust the pH between the ranges of 7 to 7.5. Collagen solution was placed on ice, to minimize cross-linking, while a 2.5 mg/mL suspension, in phosphate-buffered saline (PBS) containing 0.1 w/v % bovine serum albumin (BSA), of the dye-encapsulated microparticles was prepared. The microparticle suspension was sonicated for 10 minutes to break particles clumps and later vortexed. A 111 µL aliquot of the fluorescent microparticle suspension was added to the collagen solution. Afterwards, 100 µL of the collagen mixture was dispensed onto a clean glass cover slip and left to cross-link for 1 hr. Once ready, collagen slide was used for biofilm culture under a parallel-plate flow system.

2.6. S. aureus biofilm culture and staining

The Phillips strain of *S. aureus* was first isolated from a patient with osteomyelitis [90]. The strain was selected because it forms biofilms in collagen substrates. Tryptic soy broth (TSB; Difco, Detroit, MI) was used as growth medium for the bacteria cultures. For primary cultures, 10 μL of *S. aureus* cells, collected from stocks stored at -80°C, were placed and grown in a conical flask with 50 mL of TSB at 37°C under constant agitation.

A parallel plate flow chamber, of the same type as that described in Section 2.3, was used to grow the biofilms. Primary cells were diluted to a ratio of 1:40 in 0.2 w/v % sodium azide (NaN_3) in PBS with 0.1 w/v % BSA and infused through the flow chamber at a rate of 80 min^{-1} for 6 minutes using a syringe pump. Unattached bacteria cells were rinsed away with 0.1 w/v % BSA in PBS with NaN_3 for 10 minutes at a rate of 200 min^{-1}. TSB was then flowed at a rate of 1122.4 min^{-1} for 6 hr. The flow chamber was maintained at 37°C.

For labeling the *S. aureus* cells, anti-calcineurin A (anti-CAN) $F(ab')_2$ fragments of mouse anti-monoclonal antibody (Mab3b12) were used as the primary antibody (provided by Joseph Patti; Inhibitex, Inc., Alpharetta, GA). The primary antibody was prepared with 25.4 μL of stock solution (5.9 mg/mL) and 3 mL of PBS without NaN_3 for a 50 μg/mL concentration. Afterwards, the primary antibody was infused through the flow chamber and allowed to adhere for 45 minutes. Unattached primary antibodies were rinsed away with PBS without NaN_3. Next, DyLight 488-conjugated AffiniPure $(Fab')_2$ fragment goat anti-mouse IgG (493/518 nm excitation/emission), fragment specific with minimal cross-reaction to human,

bovine, and horse serum proteins (Jackson ImmunoResearch Laboratories, Inc., West Grove, PA), was used as the secondary antibody. The secondary antibody was prepared with 100 μL of stock solution (1.5 mg/mL) and 3 mL of PBS without NaN_3 for a 50 μg/mL concentration. Like the primary antibody, the secondary antibody was infused through the flow chamber and allowed to adhere for 30 minutes. Subsequently, the unattached secondary antibodies were rinsed away with PBS with NaN_3 and the biofilm culture was imaged using fluorescence microscopy immediately.

2.7. Statistical analysis

Statistical analysis for size distribution means for the particles of the two synthesis protocols and *S.aureus* bacteria was performed using ANOVA with a cutoff of $p < 0.05$. Paired comparison between distribution means of particles was performed using Student's T-test with a cutoff of $p < 0.05$.

3. Results

3.1. Microparticle synthesis and SEM imaging

Two methods for synthesis of the fluorescence silica microparticles was considered. The first was protocol (dye-coated microparticles) consisted of the Stöber synthesis followed by fluorescent labeling of the resulting particles by immobilization of the $Ru(Ph_2phen_3)Cl_2$ and Nile blue fluorophores. The second protocol (dye-

encapsulated microparticles) consisted of addition of the two fluorophores during the Stöber synthesis to encapsulate them within the silica. After synthesis, scanning electron microscopy (SEM) was performed to compare microparticle size and morphology. Figure 8 shows electron micrographs of the microparticles yielded by both synthesis protocols. Both sets of particles were observed to be spherical in shape and to be within similar size range as *S. aureus* bacteria. The dye-coated microparticles had an average particle diameter of ~1 μm, whereas the dye-encapsulated microparticles had diameters in the sub-micron range, ~0.5 μm. *S. aureus* bacteria have an average diameter of 0.8-1 μm.

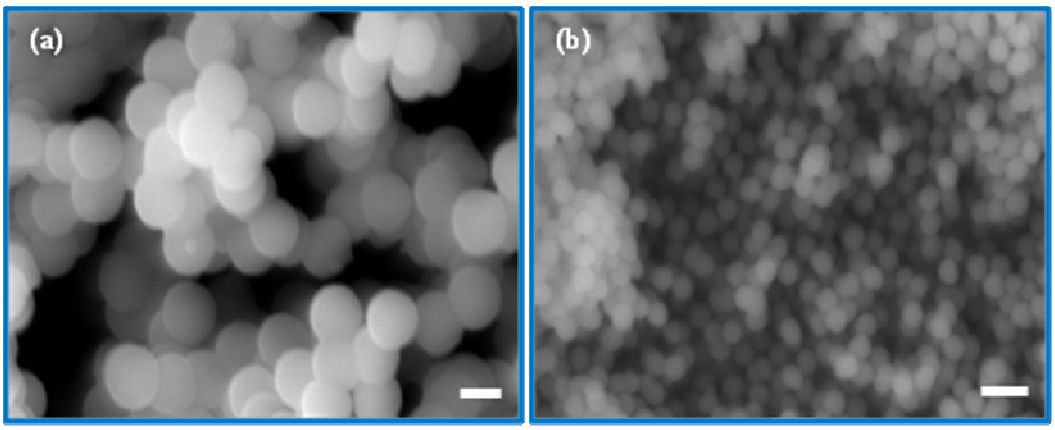

Figure 8: Scanning electron micrographs of the dye-coated microparticles **(a)** and the dye-encapsulated microparticles **(b)**. Scale bar = 1 μm.

3.2. Calibration results

The calibration of microparticle response to step-changes in oxygen concentration was performed by suspending them through the volume of the PEG-DM hydrogel. A parallel-plate flow chamber system mounted in the stage of a

fluorescence microscope was used to perform the calibration. Nitrogen and air were combined and sparged into the water reservoir to achieve step-wise increments in the aqueous dissolved oxygen concentration. The changes in microparticle fluorescence intensity were monitored by capturing fluorescence images of the sensing microparticles with the fluorescence microscope. The correlation between fluorescence intensities and dissolved oxygen content was obtained by exploring two models to fit the data for the silica microparticles for both protocols, in the partial pressure range of 0-160 mm Hg (0 to 100% oxygen saturation). Figure 9 shows the calibration with the conventional Stern-Volmer model for the two proposed synthesis protocols. For the dye-coated microparticles, regression results were 0.0024 for the Stern-Volmer quenching constant (K_{SV}, mm Hg^{-1}) and R^2 = 0.9651. For the dye-encapsulated microparticles, regression results were K_{SV} = 0.0023 mm Hg^{-1} and R^2 = 0.7505.

The second model was the two-site Stern-Volmer model, which is shown in Figure 10, also for the two proposed synthesis protocols. For the dye-coated microparticles, two-site Stern-Volmer model regression results were K_{SV} = 0.0027 mm Hg^{-1} and R^2 = 0.9684. For the dye-encapsulated microparticles, two-site Stern-Volmer model regression results were K_{SV} = 0.0081 mm Hg^{-1} and R^2 = 0.9300. Estimated values of the quenched fluorophore fraction f_1 were 0.94 ± 0.03 and 0.45 ± 0.05 for dye-coated and dye-encapsulated microparticles respectively.

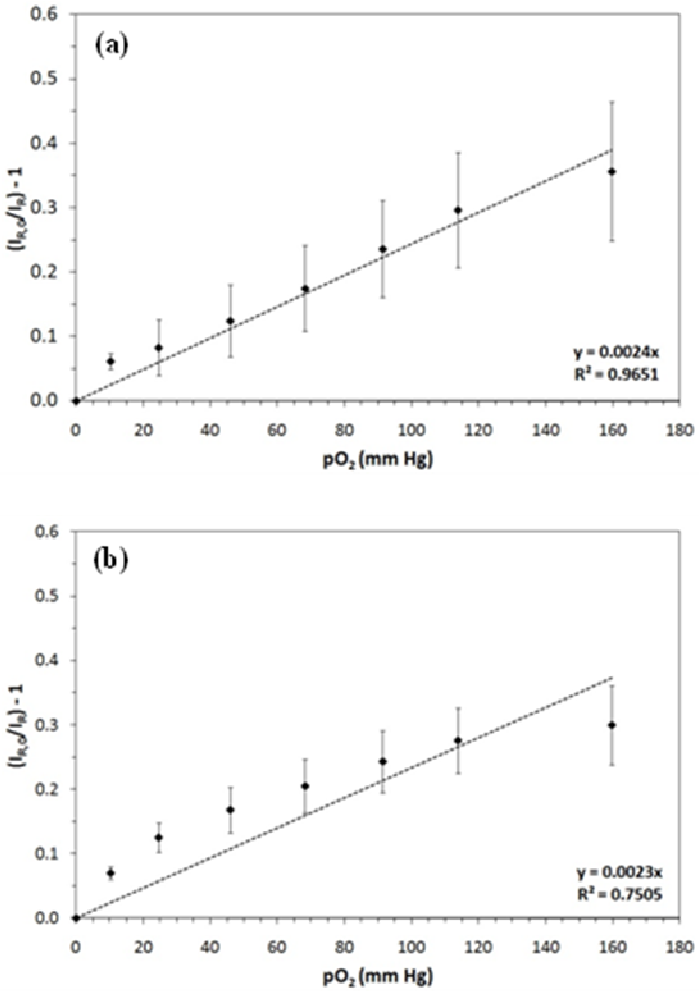

Figure 9: Conventional Stern-Volmer calibration for the dye-coated microparticles **(a)** and the dye-encapsulated microparticles **(b)**. Regression values obtained were 0.0024 and 0.0023 mm Hg^{-1} and 0.9651 and 0.7505 for the Stern-Volmer quenching constant and R^2 value dye-coated and dye-encapsulated microparticles respectively. Data shown as mean ± standard error for three trials.

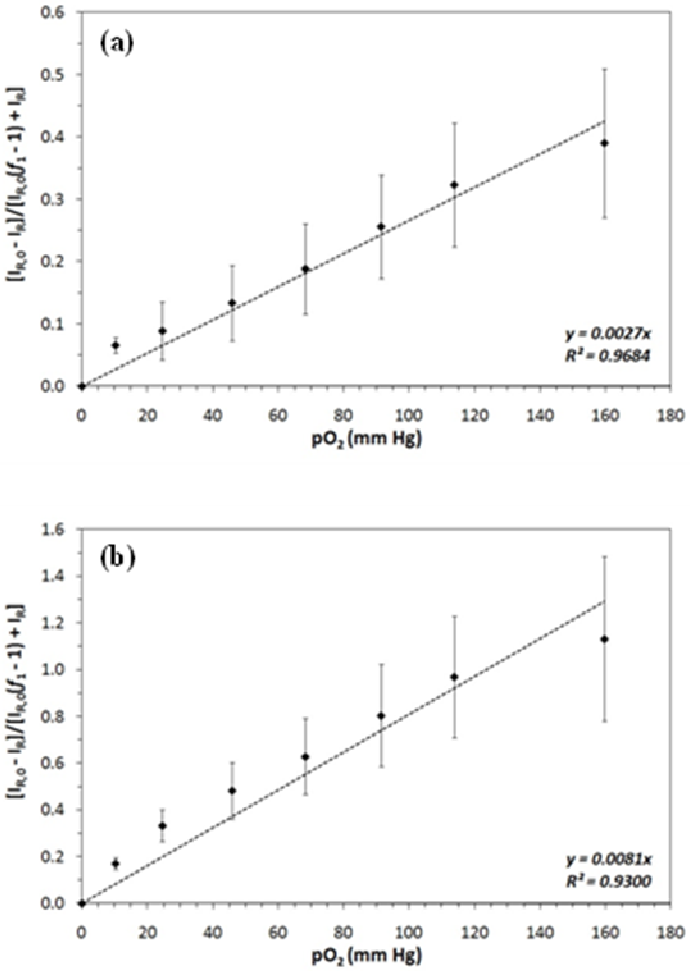

Figure 10: Two-site Stern-Volmer calibration for the dye-coated microparticles **(a)** and the dye-encapsulated microparticles **(b)**. Regression values obtained were 0.0027 and 0.0081 mm Hg^{-1} and 0.9684 and 0.9300 for the Stern-Volmer quenching constant and R^2 value for the dye-coated and dye-encapsulated microparticles respectively. Data shown as mean ± standard error for three trials.

3.3. S. aureus biofilm culture

To test the microparticles' ability to be cultured within the volume of the biofilm and we established a method to simultaneously culture the biofilm within a collage gel containing the microparticles. The substrate contained 111 μL of a 2.5

mg/mL suspension of the dye-encapsulated microparticles. Figure 11 shows fluorescence images of the *S. aureus* biofilm culture with the microparticles suspended through the volume of the collagen substrate, and indicates that microparticles and bacteria are distributed throughout a three-dimensional volume of biofilm.

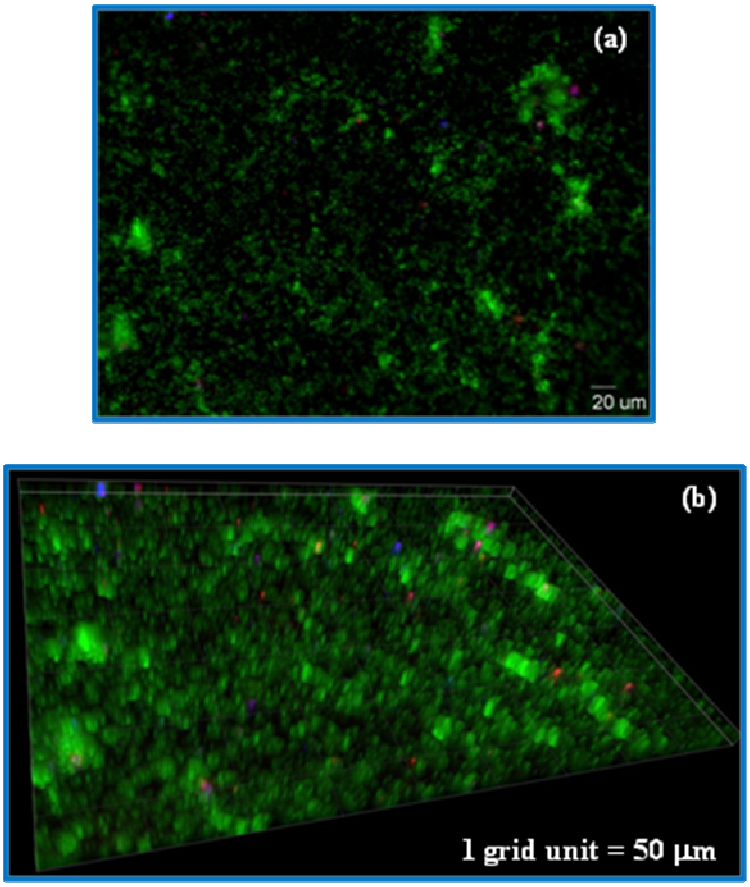

Figure 11: *Staphylococcus aureus* biofilm cultured on 2 mg/mL collagen gel containing 2.5 mg/mL of the dye-encapsulated microparticles. **(a)** 2D image depicting the surface of the biofilm. **(b)** Three-dimensonal reconstruction of the biofilm/particle system. Green fluorescence corresponds to the Dylight 488 secondary anti-body used to stain the bacteria, red fluorescence corresponds to $Ru(Ph_2phen_3)Cl_2$, and blue pseudo-color corresponds to Nile blue chloride. Magnification = 20x.

4. Discussion

Here, we developed a new method to utilize fluorescent silica microparticles for the measurement of oxygen concentration through the volume of *S. aureus* biofilms. A thorough understanding of not just the mechanism behind biofilm formation, proliferation, and planktonic-cell detachment, but also an understanding of oxygen transport through the volume of a biofilm is vital for the development of new and effective infection therapies. Thus, the described approach could prove to be an effective tool to aid in this area of investigation. We evaluated two protocols, which were based on the Stöber synthesis of silica microparticles. The first protocol immobilized the fluorophores $Ru(Ph_2phen_3)Cl_2$ and Nile blue chloride onto the surface of the synthesized microparticles. The second protocol yielded microparticles with the two fluorophores encapsulated within. The immobilization process used for the dye-coated microparticles was adapted from John et al. [61], who immobilized $Ru(Ph_2phen_3)Cl_2$ and the reference fluorophore safranin onto silica gel. In contrast, we used Nile blue chloride as our reference fluorophore due to the fact that safranin's emission spectrum overlaps with that of $Ru(Ph_2phen_3)Cl_2$. The differing emission spectra between the $Ru(Ph_2phen_3)Cl_2$ and the Nile blue chloride allowed us to independently measure their fluorescence via microscopy. $Ru(Ph_2phen_3)Cl_2$ was chosen because of its high quantum yield, high oxygen quenching, and thermal stability at 37°C [57, 80].

We compared the size and morphology of the two types of microparticles with scanning electron microscopy. As shown in Figure 8, the size range of both sets of microparticles is suitable for the desired application, as it is close to the size of the

bacteria. Furthermore, the small size range of the microparticles will minimize diffusion limitations from the medium to the fluorophores and significantly reduce response time [64, 83]. Still, both types of microparticles show a narrow size distribution. With the Stöber reaction, monodisperse silica particles can be synthesized with high fidelity for size ranges up to 0.8 μm. However, it has proven difficult to obtain monodisperse particles with larger diameters. Figure 8a demonstrates that the synthesis protocol for the dye-coated microparticles yielded spherical microparticles with a relatively monodisperse size distribution in the 1 μm size range.

The calibration of the fluorescent microparticles inside a three-dimensional PEG-DM hydrogel was carried out using a parallel-plate flow chamber mounted on the stage of a fluorescence microscope. This flow chamber system allowed for direct control over dissolved oxygen in the hydrogel/microparticle environment, as well as measurements of the changes in microparticle fluorescence intensity. Figure 9 shows a comparison between the calibrations for the two proposed synthesis protocols. The conventional Stern-Volmer model, which pertains to the fluorophores in solution, predicts a linear response of the $Ru(Ph_2phen_3)Cl_2$ fluorophore to oxygen. The dye-coated microparticles, as observed in Figure 9a, follow the conventional model with some fidelity. However, as can be observed in Figure 9b, the dye encapsulated microparticles do not. In fact, they exhibit a downward curvature, mimicking a second order response, which suggests heterogeneities in the carrier structure or a non-uniform distribution of fluorophore molecules throughout the carrier matrix [56, 58, 80]. Rossi et al. postulated that the quenching efficiency of $Ru(Ph_2phen_3)Cl_2$

decreases significantly when encapsulated within silica particles synthesized using the Stöber synthesis [70]. Yet, the process enhances its stability and emission intensity because encapsulation will reduce the fluorophore's exposure to oxygen molecules present in the environment. Particle size also plays an important role in quenching efficiency, as smaller particles have lower surface area for the immobilization of dye molecules and for the transport of oxygen molecules to any fluorophores contained within. This phenomenon is less present when $Ru(Ph_2phen_3)Cl_2$ is immobilized onto silica carriers of larger size [88].

It is important to mention that for the dye-encapsulated microparticles additional TEOS was not added drop-wise to the ongoing reaction. The drop-wise addition of the TEOS promotes growth on the surface of the pre-formed particles increasing their size; hence, why the dye-coated microparticles appear larger. If such as step would have been performed for the second protocol, we hypothesize that the Stern-Volmer model would have deviated from linearity even further, as the thick layer of silica material would have prevented oxygen molecules from accessing the encapsulated fluorophores even more.

The fraction of quenchable fluorophore (f_1) gives even greater insight into this matter. Results from the calibration using the two-site Stern-Volmer model, reveals that for the dye-encapsulated microparticles $f_1 = 0.45 \pm 0.05$, whereas $f_1 = 0.94 \pm 0.03$ for the coated microparticles particles. The fraction of quenchable fluorophore (f_1) is a measure of the oxygen accessibility to $Ru(Ph_2phen_3)Cl_2$ molecules. This means that for the dye-encapsulated microparticles, less than half of the $Ru(Ph_2phen_3)Cl_2$ is available for quenching reducing their efficacy as sensors, but enhancing our ability

to see them with microscopy due to their enhanced emission intensity. In contrast, the dye-coated microparticles are better as sensors due to their sensitivity, derived from the accessibility of $Ru(Ph_2phen_3)Cl_2$ molecules.

We selected the dye-encapsulated microparticles to develop a method to simultaneously characterize the oxygen-sensing microparticles and biofilm structure due to their enhanced emission intensity. These proof-of-concept experiments lay the foundation for quantitative characterization of oxygen concentration within complex biofilm structures.

5. Conclusions

We have introduced the development of monodisperse micron-sized fluorescent silica particles synthesized using two adaptations of the Stöber synthesis, aimed at applications for the monitoring of oxygen transport within *S. aureus* biofilms. One protocol yielded particles with the fluorophores $Ru(Ph_2phen_3)Cl_2$ and Nile blue chloride immobilized on the surface, while the other encapsulated of the fluorophores within the microparticles. After synthesis, both types of microparticles exhibited a size range similar to that of *S. aureus* bacteria. Both types of microparticles were also calibrated using a parallel-plate flow chamber system mounted on a fluorescence microscopy stage. Both protocols yielded particles that were effective for measuring oxygen concentration via fluorescence microscopy. Calibration by the conventional and two-site Stern-Volmer models provided insight into fluorophore distribution with the particles and their accessibility to oxygen molecules on the particle microenvironment. Finally, the microparticles were cultured

within *S. aureus* biofilms demonstrating their potential for future in depth studies of oxygen diffusivity within biofilms of various structures.

CHAPTER 4: Fluorescent microparticles for sensing tumor cell response to oxygen levels within 3D scaffolds

1. Introduction

Oxygen diffusion through biomaterial scaffolds plays an important role in maintaining healthy tissues. Oxygen supply is a limiting factor during the growth of highly metabolic tissues and large tissue masses, mainly as a result of the lack of vascularization in tissues cultured in vitro and the low solubility of oxygen in the culture medium. Therefore, gaining an understanding of the cellular response to changes in soluble cues, such as oxygen concentration, through their biomaterial microenvironment may potentially lead to improving methods for control over cell behavior in tissue engineering [1]. Unfortunately, few methods exist that allow for direct correlation between spatial changes in oxygen concentration through a biomaterial scaffold and their impact on cellular function.

To address this need, we have developed fluorescent oxygen-sensing microparticles that can be suspended in any transparent biomaterial scaffold used in cell culture and tissue engineering [88]. Application of the sensing microparticles for investigating cellular response to changes in oxygen concentration through biomaterial scaffolds will incorporate simultaneous monitoring of the microparticle response and cellular function. However, in order to specifically correlate cellular response to gradients in oxygen concentration, measurement of a response that is triggered only by fluctuations in oxygen optimal. Moreover, this response should be directly related to how cells mediate their function under such conditions. Not all

measurements of protein products or metabolic activity are direct indicators of the cells' response to oxygen concentration due to the fact that they may simultaneously change with fluctuations in other cues from the microenvironment such nutrient content, temperature, pH, and the presence of toxic species.

The helix-loop-helix transcription factor, HIF-1, which is composed of two subunits, HIF-1α and HIF-1β, is directly controlled by hypoxia in the cellular environment. During normoxic conditions, HIF-1α is continuously degraded by the ubiquitin-proteome system. This degradation process is oxygen-dependent, as under hypoxic conditions HIF-1α is no longer degraded and is translocated to the cell nucleus where it binds with the hypoxia-inducible factor-1β (HIF-1β) to form HIF-1 [22, 91]. Thus, HIF-1α is great target molecule for directly correlating cellular function to oxygen concentration. Measurements of HIF-1α may be considered direct, as they provide could insight into how cells mediate their response to hypoxia and specific oxygen concentrations that regulate these processes.

Herein, we present the preliminary characterization of murine 4T1 mammary carcinoma, human C8161 subcutaneous melanoma, and human U2OS osteosarcoma cells transfected to produce a pEGFP-HIF-1α fusion protein. We demonstrate that while the cells were successfully transfected, the transport of the pEGFP-HIF-1α fusion was not comparable to that of conventional HIF-1α in non-transfected cells, as porposed by Wotzlaw et al. and Liu et al. [92, 93]. These preliminary studies contribute to the development a methodology based on the oxygen-sensing microparticles and the transfected cell lines to simultaneously monitor particle and cellular fluorescence and correlate local oxygen concentration to cell response. This

correlation would have provided insight into (1) oxygen transport through the hydrogel scaffold during cell culture, and (2) what oxygen concentrations impact cellular functions in 3D culture.

2. Materials and methods

All chemical reagents were purchased from Fischer Scientific or Sigma-Aldrich, and all cell culture materials were purchased from Invitrogen, unless otherwise stated.

2.1. Cell culture

Murine 4T1 mammary carcinoma cells were cultured in IMDM supplemented with 10 vol. % fetal calf serum (Hyclone Laboratories, Logan, UT), 1 vol. % of 5,000 (i.u. M/L)/5,000 (u.g./mL) penicillin/streptomycin, 1 vol. % of 0.2 M Glutamax, and 0.1 vol. % 50 mg/mL Gentamycin.

Human C8161 subcutaneous melanoma cells were cultured in RPMI supplemented with 10 vol. % defined fetal bovine serum (Hyclone Laboratories, Logan, UT), 1 vol. % 5,000 (i.u. M/L)/5,000 (u.g/mL) penicillin/streptomycin, 1 vol. % 0.05 mM β-mercaptoethanol (Mallinckrodt Baker, Phillipsburg, NJ), 1 vol. % 1 M HEPES, 1 vol. % 0.2 M Glutamax, 0.1 vol. % 50 mg/mL Gentamycin, 0.02 vol. % 25 mg/mL Plasmocin.

Human U2OS osteosarcoma cells were cultured in DMEM supplemented with 10 vol. % defined fetal bovine serum (Hyclone Laboratories, Logan, UT), 1 vol. %

5,000 (i.u. M/L)/5,000 (u.g/mL) penicillin/streptomycin, 1 vol. % 0.2 M Glutamax, and 0.1 vol. % 50 mg/mL Gentamycin.

For selection of the transfected cells, 0.016 vol. % 1 mg/mL G418 (Geneticin; EMD Biosciences, San Diego, CA) was added to the culture medium. Transfected cells were cultured in 0.8 cm^2-wells of a plastic chambered slide (Lab-Tek Chamber Slide system; Fisher, Pittsburgh, PA) at a density of 5,000 cells/well (6250 cells/cm^2). Hypoxic incubation was carried out inside a hypoxic in vitro cabinet (Coy Laboratory Products, Grass Lake, MI), where the cells were subjected to an atmosphere of 5% CO_2, 94% N_2, and 1% O_2 at 37°C. The cabinet is housed within a conventional CO_2 incubator. Cells were incubated under hypoxia for 8 hours. Control cells were culture outside of cabinet, i.e. cultured under normoxic conditions. The 8 hour time point was selected in accordance to previous findings by Wang et al. [91] and Genetos et al. [94], that demonstrated HIF-1α expression to be maximal in the 4-8 hour range during hypoxic culture of Hep 3B and PC-12 cells.

2.2. Plasmids and stable transfections

Full length HIF-1α transcript DNA coding sequence was graciously donated by Dr. Joachim Fandrey and his research group from the University of Duisburg-Essen (Essen, Germany) [92]. The sequence was ligated into pEGFP-C1 (Clontech, Palo Alto, CA). The pEGFP-HIF-1α plasmid was sequenced. Sequencing results revealing that the GFP and HIF-1α were in frame. In addition, a NCBI Blast query using the nucleotide sequence from the obtained HIF-1α DNA revealed that it was a 97% match to human HIF-1α transcript DNA. All cells were transfected by

electroporation using the Amaxa Nucleofactor system (Lonza, Walkersville, MD) and grown for 48 hours after transfection. After 48 hours, the cells were transferred to a culture flask and cultured as described in Section 2.1 for selection.

2.3. Microscopy and image analysis

Immediately after the 8-hour period of hypoxic incubation, the cells were fixed with 4 vol. % formaldehyde for 30 minutes at 37°C. Subsequently, cell nuclei were stained with 3 nM 4',6-diamino-2-phenylindole (DAPI) and the cytoskeletal protein F-actin, was stained with phalloidin Texas Red-X (300 U).

Imaging was carried out with an IX-81 fluorescence microscope (Olympus, Center Valley, PA). Image analysis for cell count and HIF-1α expression was conducted NIH-ImageJ freeware. Two protocols for image analysis were employed. First, total overall fluorescence was evaluated using line scans across the width of a particular image, which yielded an average value of the grayscale intensity from pEGFP-HIF-1α for that image. Each image was segmented with a series of line profiles from which the average value of intensity was determined. The image analysis performed this way represented a global measurement of fluorescence intensity across the image area. The second protocol measured the total area occupied by the pEGFP-HIF-1α fluorescence, and the total grayscale intensity, as normalized to that for F-actin occupied area and fluorescence. Both protocols described above were written as custom analysis MACRO's within the ImageJ interface.

2.4. Statistical analysis

Statistical analysis for hypoxia experiments was performed using the Student's T-test, with a cutoff of $p < 0.05$, as an unpaired comparison between area and intensity for the control and 8-hour time points.

3. Results

To study the expression of the HIF-1α under hypoxic conditions, 4T1, C8161, and U2OS cells were transfected to produce a pEGFP-HIF-1α fusion and cultured under hypoxia for 8 hours. Imaging results for all three cells types after transfection are shown on Figures 12 and 13. Figure 12 displays images of the control, showing that pEGFP-HIF-1α fluorescence was not inside the cell nucleus. From Figure 13, it can be observed that the pEGFP-HIF-1α fluorescence was not inside the cell nucleus either after 8 hours of hypoxic culture. In both cases, pEGFP-HIF-1α fluorescence appears diffused throughout the body of the cell.

As a secondary evaluation of the results of the transfection, overall mean pEGFP-HIF-1α intensity, area of fluorescence, and the intensity of the fluorescence area were measured using image analysis. All measurements were also normalized to cell number. Figure 14 shows image analysis results for overall mean grayscale intensity. Statistical analysis performed using Student's T-test ($p < 0.05$) demonstrated that for 4T1 and U2OS cells there was no statistical difference in intensity between the control and 8 hours. For the C8161 cells however, there was an observed increase of 15.2% in intensity at 8 hours of hypoxia.

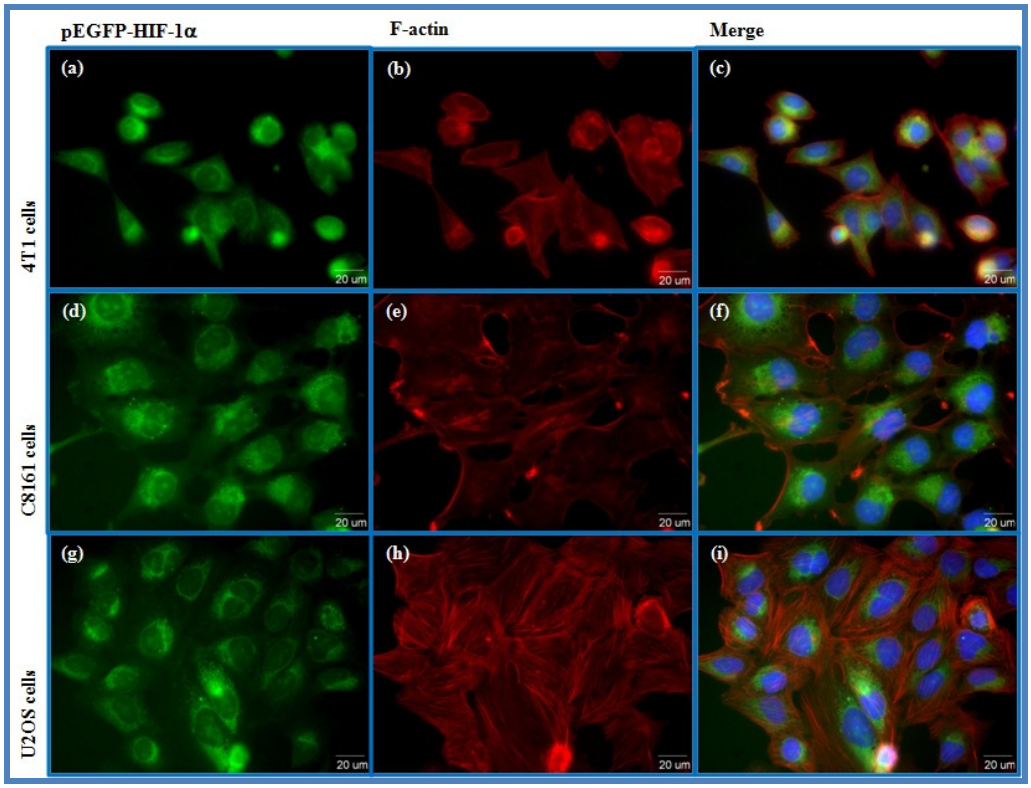

Figure 12: Fluorescence imaging results for 4T1, C8161, and U2OS control. Images **(a)**, **(d)**, and **(g)** show pEGFP-HIF-1α fluorescence fusion; images **(b)**, **(e)**, and **(h)** show F-actin staining; and images **(c)**, **(f)**, and **(i)** show pEGFP-HIF-1α, F-actin staining (Texas Red), and DAPI staining overlaid. Scale bar = 20 μm.

Image analysis was performed to measure the area of pEGFP-HIF-1α fluorescence (Figure 15a). A ratio of the normalized pEGFP-HIF-1α area to that of F-actin was calculated. Statistical analysis demonstrated that was no difference in the area of pEGFP-HIF-1α fluorescence for any of the three cell types between the control and 8 hours of hypoxic culture. Image analysis was also performed for measuring the intensity of the pEGFP-HIF-1α area (Figure 15b). A ratio of the normalized intensity of the pEGFP-HIF-1α area to that of F-actin was calculated.

Statistical analysis demonstrated that for 4T1 and U2OS cells there was no difference in intensity for the selected area of pEGFP-HIF-1α fluorescence between the control and 8 hours of hypoxic culture. For the C8161 cells, there was an observed increase of 20.2% in intensity the pEGFP-HIF-1α fluorescence area at 8 hours of hypoxia.

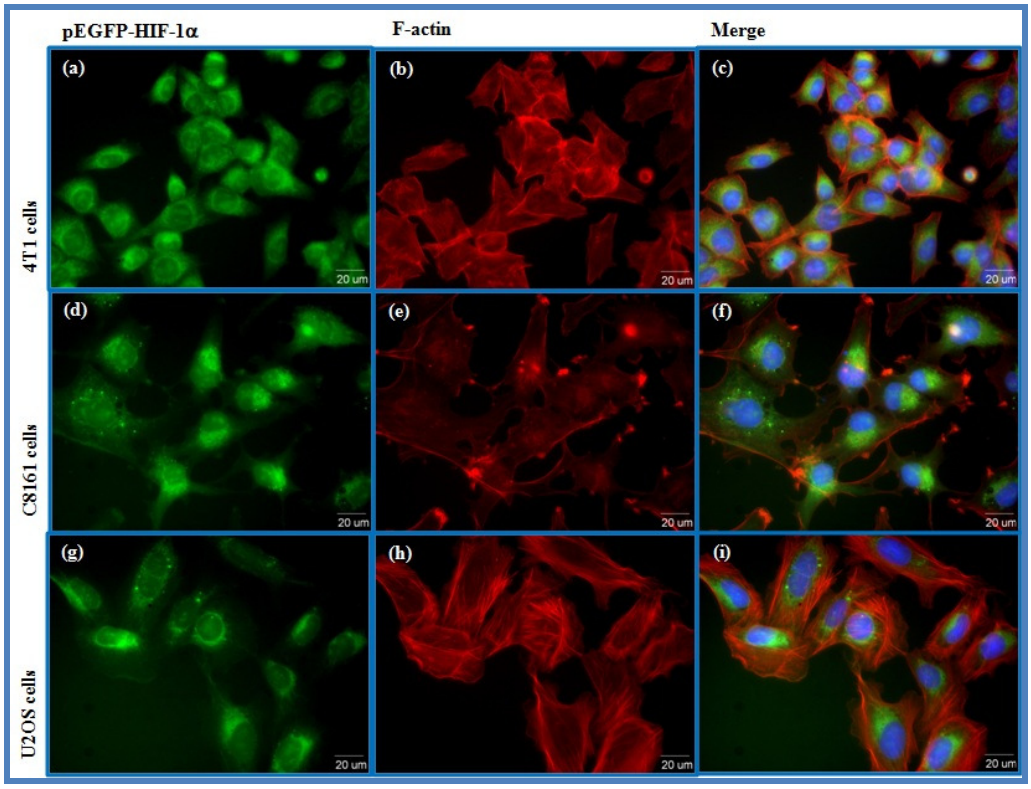

Figure 13: Fluorescence imaging results for 4T1, C8161, and U2OS for 8 hour time point. Images **(a)**, **(d)**, and **(g)** show pEGFP-HIF-1α fluorescence; images **(b)**, **(e)**, and **(h)** show F-actin staining; and images **(c)**, **(f)**, and **(i)** show pEGFP-HIF-1α, F-actin staining (Texas Red), and DAPI staining overlaid. Scale bar = 20 μm.

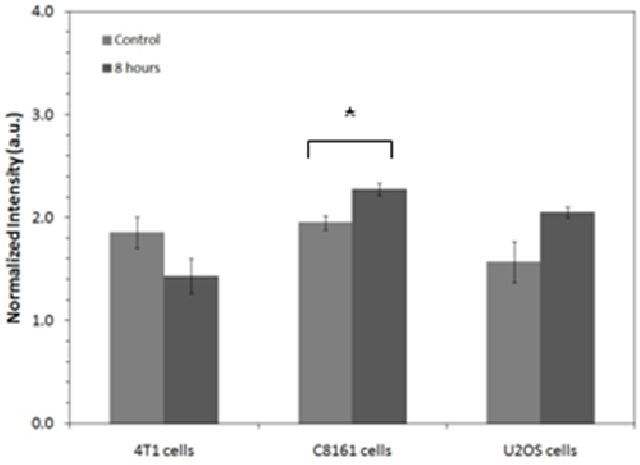

Figure 14: Results for overall mean grayscale intensity measured with image analysis. Student's T-test results indicated that for 4T1 and U2OS cells there was no difference in intensity between the control and 8 hours. For C8161 cells, there was an observed increase of 15.2% in intensity at 8 hours of hypoxia. Data shown as mean ± standard error for four trials.

4. Discussion

Our approach was inspired by published works by Wotzlaw et al. and Liu et al. [92, 93], where fusions of fluorescent proteins and HIF-1α were observed within the cell nucleus. In Wotzlaw's work, human U2OS osteosarcoma cells were transfected to express the HIF-1α-cyan fluorescent protein (pECFP-HIF-1α) and HIF-1β-yellow fluorescent protein (pEYFP-HIF-1b) fusions [92]. Under hypoxia, the pECFP-HIF-1α fusion protein transferred to the cell nucleus where it united with the pEYFP-HIF-1β fusion to form HIF-1 (Figure 16). This process allowed the study of HIF-1 complex activity using fluorescence resonance energy transfer (FRET) between the two fluorescent markers and estimate the distance between the two HIF-1 subunits.

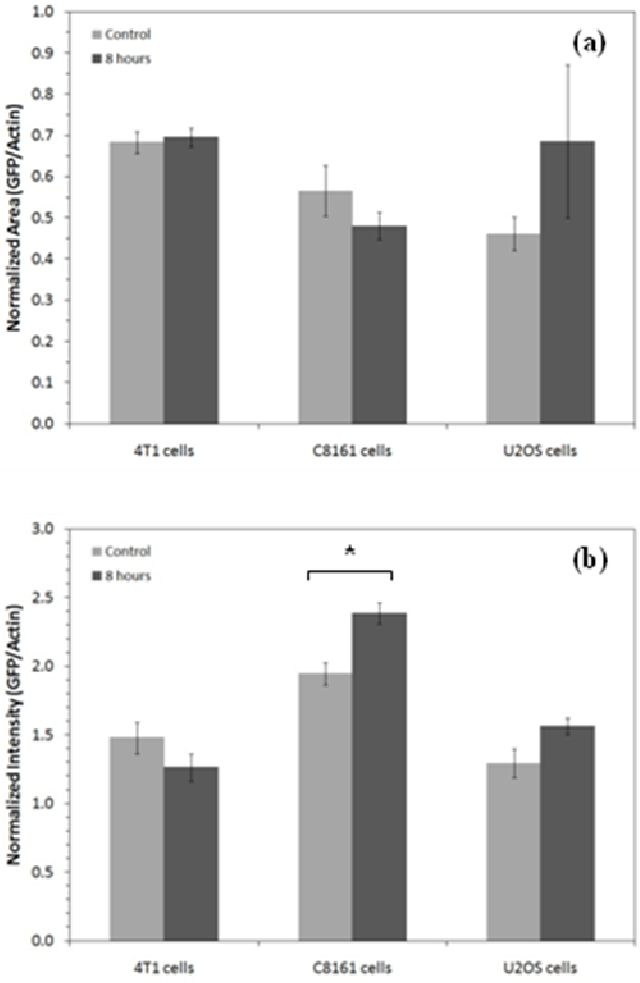

Figure 15: (a) Results for image analysis of pEGFP-HIF-1α fluorescence area. T-test results indicated that there was no statistical difference in the area coverage by pEGFP-HIF-1α fluorescence, for any of the three cell types, between the control and 8 hours of hypoxia. **(b)** Results for image analysis of pEGFP-HIF-1α fluorescence area intensity. T-test results indicated that for 4T1 and U2OS cells there was no difference in pEGFP-HIF-1α fluorescence area intensity between the control and 8 hours. For the C8161 cells, there was an observed increase of 20.2% in pEGFP-HIF-1α fluorescence area intensity at 8 hours of hypoxia. Data shown as mean ± standard error for four trials.

Liu et al., transfected the human prostate cancer cell line PC-3ML to express pEGFP-HIF-1α, allowing the study of induced translocation of HIF-1α to the nucleus in the presence of the immunosuppressant prostaglandin E_2 (PGE_2) [93] (Figure 17). These results suggested that the fluorescent protein component of the fusion would not hinder its regulation. The work by Wotzlaw and Liu are just two examples out of a group of studies that employed the transfection of a mammalian cell line with a plasmid containing fluorescent protein fusions with HIF-1α [95-98]. All of which have observed the translocation of the fusion protein to the nucleus in response to their studied stimuli, further validating the hypothesis that GFP does not alter regulation of the fusion protein in comparison to its wild-type counterpart.

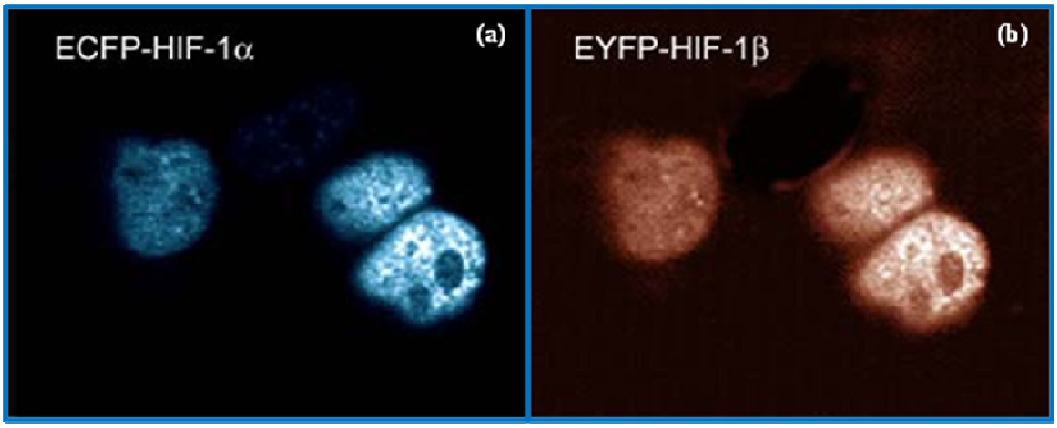

Figure 16: Human U2OS osteosarcoma cells transfected with pECFP-HIF-1α **(a)** and pEYFP-HIF-1β **(b)**. Cells were cultured and imaged with florescence microscopy under an atmosphere of 1% O_2 at 4 hours. The pECFP-HIF-1a can be seen clearly inside the cell nucleus. Images were kindly donated by Dr. Joachim Fandrey and his research group from the University of Duisburg-Essen (Essen, Germany).

We studied the effects of hypoxia on three cell types that were transfected to express a pEGFP-HIF-1α fusion. Figures 13 displays fluorescence images of the 4T1,

C8161, and U2OS cells after 8 hours of culture under an atmosphere of 1% O_2. The fusion protein was expected to be seen inside the cell nucleus. However, there was no appreciable change in the location of the fluorescence from the fusion, as it was mostly diffuse across the cell body. The fusion protein was observed to be more concentrated around perimeter of the cell nucleus, giving rise to the hypothesis that the GFP was not entering the nucleus. As described above, studies that have employed this technique in the past have not seen evidence of this phenomenon. Thus, it instills the possibilities that either our transfection did not occur as expected, or the HIF-1α transcript DNA was not expanded or ligated correctly. As described in Section 2.2, sequencing results demonstrated that GFP and HIF-1α transcript DNA were in frame, assuring that the correct ligation of the transcript DNA to the plasmid. Secondly, from Figures 12 and 13 we can see that GFP fluorescence is present, affirming that the transfection occurred. Furthermore, all cell types exhibited resistance to the G418 antibiotic, affirming that the plasmid was incorporated into the host genome.

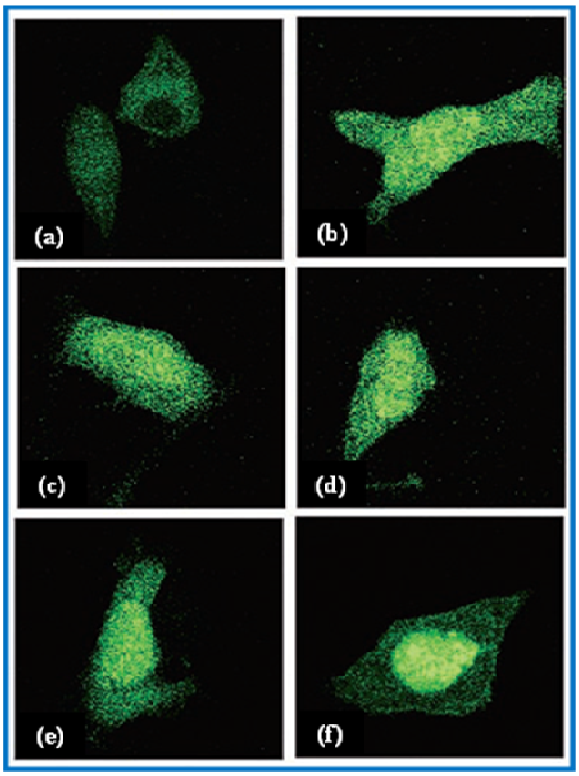

Figure 17: PC-3ML cells transfected with pEGFP-HIF-1α. The cells were treated with 1 mM PE_2 for **(b)** 4 hr, **(c)** 6 hr, **(d)** 8hr, **(e)** 12 hr, and **(f)** 16 hr. **(a)** Represents control. After treatment, pEGFP-HIF-1α fusion can be observed slowly being transported from the cytoplasm to the cell nucleus. Figure was adapted from Liu et al. [93].

Two approaches were developed to analyze image fluorescence in an unbiased manner. One measured overall image fluorescence, while the other determined the area of pEGFP-HIF-1α fluorescence and the intensity exhibited by that area. We hypothesized that culture under hypoxic conditions would result in increased fusion protein fluorescence, given that its stabilization under hypoxic conditions prevents its degradation. Also, as the HIF-1α was transported to the nucleus, we hypothesized that pEGFP-HIF-1α fluorescence would be higher at the cell nuclei. Hence, by measuring the area corresponding to pEGFP-HIF-1α fluorescence for both the control

and the 8 hour time point, an appreciable change in the area of pEGFP-HIF-1α fluorescence and its intensity due to accumulation was expected. There was no statistical difference between the conditions for the 4T1 and U2OS cells as measured by total fluorescence (Figure 14) or by intensity normalized by cell area (Figure 15b). This means that the fusion protein was not transported to the nucleus upon exposure to hypoxia, or it did not accumulate under these conditions. The C8161 cells exhibited a statistical difference in the overall fluorescence of pEGFP-HIF-1α and the intensity of the area occupied by pEGFP-HIF-1α between the control and 8 hour time point, but no statistical difference for the area occupied by the pEGFP-HIF-1α. While the latter result hints at the accumulation of the fusion protein for the C8161 cells, it did not translocate expected.

5. Conclusions

We have described preliminary characterization of three tumor cell lines transfected to express a pEGFP-HIF-1α fusion protein. These cells were developed to work in conjunction with oxygen-sensitive microparticles for the characterization of cell response to gradients in oxygen concentration existing through the volume of a biomaterial scaffold during 3D culture. Transfected cells were cultured in hypoxic conditions for up to 8 hours. The cells were expected to exhibit fluorescence of the fusion protein inside the nucleus after 8 hours of hypoxic culture. However, no fluorescence from the pEGFP-HIF-1α fusion was observed inside the nucleus. Fluorescence was either diffused through the body of the cell, or accumulated at the perimeter of the cell nuclei for both the control and the 8 hour time point. To

characterize these results, two image analysis protocols were developed to measure (1) the overall intensity of the pEGFP-HIF-1α fusion and (2) the area occupied by the fusion and its intensity. For 4T1 and U2OS cells no statistical differences were observed for overall intensity, area, and area intensity for both the control and the 8 hour time point. For C8161 cells, statistical differences were observed for the overall intensity and area intensity, but no statistical differences were observed for area of fluorescence. These results were conflicting with expectations set from their comparison to previous studies where fusion protein fluorescence was observed strictly within the cell nucleus during hypoxic culture.

CHAPTER 5: Conclusions and future directions

1. Summary of presented work

The work presented here highlights our efforts at the adaptation and application of fluorescence quenching technologies towards the characterization of oxygen transport through biomaterials and the investigation of cellular response to changes in oxygen concentration. These efforts concerned mainly the translation of fluorescence quenching to microparticle technologies. Finally, we showed our preliminary efforts towards the development of a reporter protein within mammalian cells that could be employed towards the simultaneous correlation of oxygen concentration and cellular response during 3D culture of tissues in the presence of the developed microparticles in vitro.

Specifically, we adapted fluorescence quenching technology into two microparticle approaches, one for use in mammalian cell culture and the other for use in bacterial culture. Both employed the immobilization of two fluorophores, $Ru(Ph_2phen_3)Cl_2$ and the Nile blue chloride, onto silica carriers. The difference between the two, however, was most evident in their size. One set of particles was developed using commercially available silica gel, in the size range of 9.5-11 μm, for applications concerning mammalian cell culture; whereas, the other set was developed using particles synthesized with the Stöber reaction, for applications concerning bacterial biofilms. Additionally, the larger microparticles were encapsulated within a non-cytotoxic polymer, poly (dimethylsiloxane) (PDMS), to ensure that they would not cause harm to mammalian cells during culture. Both sets

of particles were demonstrated to be suitable as oxygen sensors and be suspended through the volume of transparent biomaterial scaffolds during cell culture. In the following sections, the reader will find information regarding future application plans for the developed oxygen sensing microparticles presented in the previous chapters.

2. Fluorescent oxygen-sensing microparticles and the simultaneous correlation between oxygen concentration and cell response

In Chapter 2, we presented the development and the characterization of oxygen-sensitive microparticles designed from fluorophore-bound silica gel particles encapsulated within PDMS. We demonstrated that not only where these particles non-cytotoxic to cells, they were also roughly in the same size as mammalian cells and capable of sensing oxygen concentration in ranges relevant to mammalian cells culture. Later in Chapter 5, we presented our preliminary efforts to develop a series of tumor cell lines that express a pEGFP-HIF-1α fusion protein. HIF-1α was hypothesized to be suitable marker for experiments where the simultaneous monitoring of fluorescence from the microparticles and the cells could yield a direct correlation between oxygen concentration and cell response. Thus, the next step is to combine the cells with the microparticles. Specifically, we can culture the cells and microparticles simultaneously within poly(ethyleneglycol)-dimethacrylate (PEG-DM) hydrogels. Figure 18 shows a schematic of the proposed strategy.

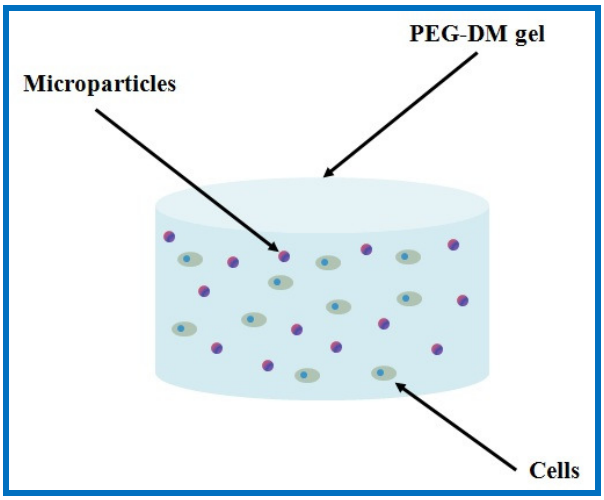

Figure 18: Schematic of proposed experimental strategy for the correlation of oxygen concentration with cell response. The schematic displays the transfected cell cultured in conjunction with the fluorescent microparticles within a PEG-DM hydrogel.

We hypothesize that culturing the transfected cells and microparticles within a PEG-DM hydrogel, we will observe a gradient in oxygen concentration spanning from the surface of the hydrogel (exposed to the culture medium) to the gel interior. Fluorescence from the microparticles and from the pEGFP-HIF-1α fusion will be simultaneously monitored as a function of position within the gel. We suspect pEGFP-HIF-1α fluorescence to be diffused in the healthy cells; whereas in the gel interior, pEGFP-HIF1α fluorescence will be located predominantly inside the cell nuclei. This experiment will serve as an indicator of oxygen concentrations that specifically trigger this cellular response in complex 3D microenvironments.

3. Fluorescent microparticles for characterizing oxygen transport through Staphylococcus aureus biofilms

In Chapter 3, we presented the development and characterization of fluorescent microparticles synthesized by two adaptations of the Stöber synthesis. We demonstrated that the fluorophore immobilization method has a significant effect on their sensing function. We proposed the use of these particles for characterizing oxygen transport through *S. aureus* biofilms and performed preliminary experiments where *S. aureus* biofims were cultured in conjunction with the dye-encapsulated microparticles in a collagen gel. The results demonstrated that we can create a three-dimensional system where the microparticles are suspended not only through the volume of the collagen substrate, but also through the volume of the biofilm.

In Chapter 1 we mentioned that Cramton et al. demonstrated that anoxic conditions inside the volume a biofilm promote the production of polysaccharide intercellular adhesin (PIA) [21]. PIA has been tied to the promotion of biofilm formation and growth. Therefore, we hypothesize that experiments where *S. aureus* biofilms are cultured on a collagen substrate with fluorescent silica microparticles suspended through its volume can lead to a correlation between PIA expression and oxygen transport. This correlation may be built with simultaneous monitoring of fluorescence from the anti-body labeled PIA and from the microparticles. This correlation will lead to an increased understanding of PIA expression and distribution through *S. aureus* biofilms in relation to oxygen transport.

4. Closing statements

In this chapter we have presented several strategies for the progression of the projects and experiments presented through this dissertation. These strategies seek to expand the applications of the developed microparticles in a range of topics, by making use of their unique characteristics. We hypothesize these proposed strategies will propel the highlighted microparticles and PEG-DM hydrogels forward within the tissue engineering and biomaterial fields.

APPENDIX: Image analysis protocols

The following is a detailed description of the protocols utilized for image analysis. NIH ImageJ freeware was employed for the acquisition of data for several of the experiments described in this thesis. We will start with the acquisition of cell number and density for the cytotoxicity of mouse balb 3T3 fibroblasts described in Chapter 2. Subsequently, we will describe the use of line scans for evaluating overall grayscale intensity and the use of threshold selections for measuring pEGFP-HIF-1α fluorescence and its occupied area.

1. Image analysis protocol for the acquisition of cell number and density in 3T3 mouse fibroblasts cytotoxicity experiments

The cell number was obtained by employing a custom written MACRO within the ImageJ freeware. Cell nuclei were imaged a 10x magnification. At this magnification, the length to pixel ratio is 0.645 μm/pixel and the size of the total imaged area was 887.5 x 600.48 μm (5.33×10^{-3} cm^2). The length to pixel ratio is an important value that must be applied as a scale to every image analyzed; otherwise, the proposed MACRO will not work properly. It is important to note, that the length to pixel ratio will depend on the magnification used during imaging. To set a global scale for analyzing images, select the "*Set Scale*" command from the "*Analyze*" menu tab within the ImageJ interface. Once the new menu appears, insert the known ratio and the desired units – in this case, units of μm were used for all analysis protocols.

With knowledge of the cell number, an areal density was calculated by obtaining the ratio of the cell number to the imaged area. The coding for the MACRO is shown in Figure 19.

```
setAutoThreshold();
  run("Threshold...");
run("Convert to Mask");
run("Watershed");
run("Analyze Particles...", "size=20-Infinity circularity=0.00-1.00 show=Ellipses display exclude clear include summarize");
```

Figure 19: Coding for cell-counting MACRO in NIH ImageJ freeware. The coding was written to account for circular objects of a size range from 20 to infinity. This numerically assigned value range corresponds to object diameters of 5 μm and beyond. Additionally, the "*Watershed*" function breaks objects that are perceived as being clustered together. Objects adjacent to the edge of the imaged area were not accounted for.

To obtain the cell count, first the desired image is opened with the ImageJ software (Figure 20). Then, the MACRO is applied to the image by selecting "*Run MACRO*" command from the "*MACRO*" menu tab. The software proceeds to report (1) a summary of the counts and (2) a visual representation of the objects counted that meet the constraints set by the written MACRO. Figure 21, depicts both these results.

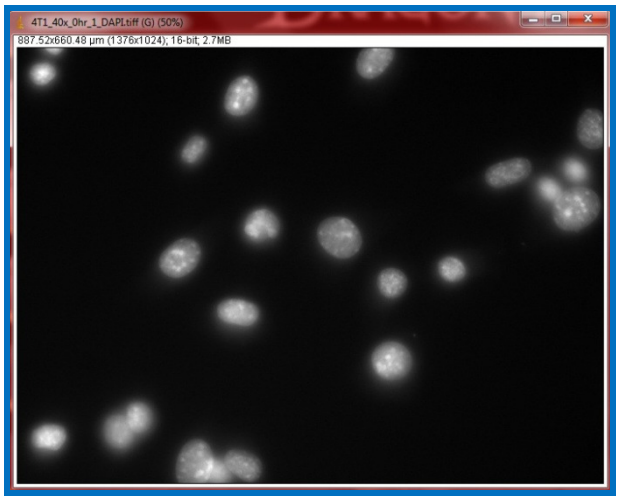

Figure 20: Image of DAPI stained cell nuclei as opened with ImageJ.

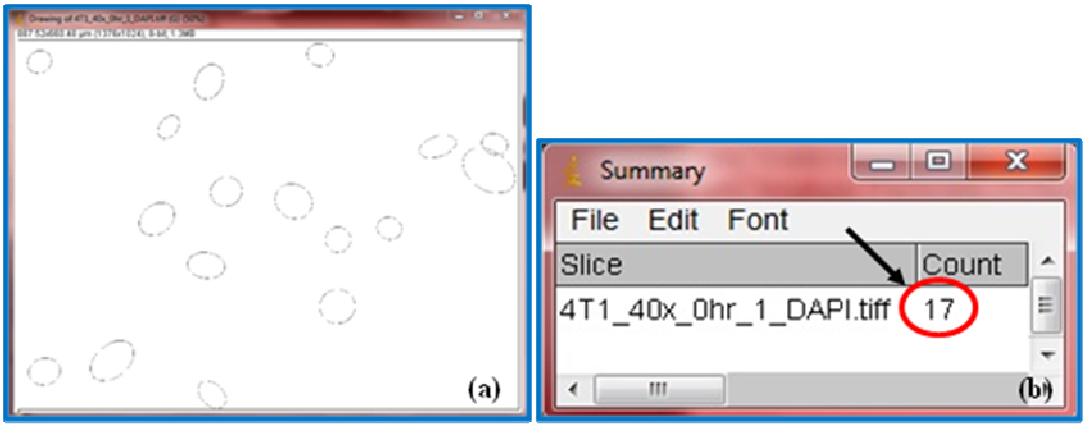

Figure 21: Results from cell-counting MACRO after it is applied to an opened image of cell nuclei. **(a)** Image representing the selected objects that were accounted for by MACRO. **(b)** Summary of results. The black arrow points to the cell count as given by results – circled in red.

Finally, as mentioned above, the counted number of cells was normalized to the image area (in cm^2) to obtain the cell density results shown in Figure 5 (Chapter 2).

2. Image analysis and line scan protocol for measuring overall grayscale intensity

Images taken of the fluorescent microparticles during calibration and reversibility experiments were taken at 4x magnification. At this magnification, the length to pixel ratio is 1.6125 µm/pixel and the size of the total imaged area was 2218 x 1651 µm. To obtain the measurements of overall grayscale intensity from the images, we begin by opening the desired time point with ImageJ (Figure 22).

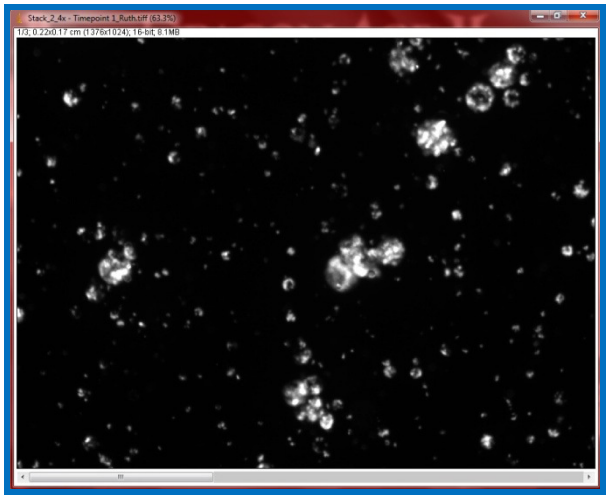

Figure 22: Image of oxygen-sensing microparticles within PEG-DM hydrogel substrate as opened with ImageJ.

Next, a custom MACRO is applied to the image. The MACRO sections the image into 21 parts of equal size. Each line counts all fluorescent objects it crosses in its path, from which the software gives a mean value of intensity for those objects. Therefore, results for each application of the MACRO are for each of the 21 lines sectioning the opened image. An average intensity is obtained for the opened image,

i.e. the considered time point, by proceeding to average the 21 results given by the application of the MACRO.

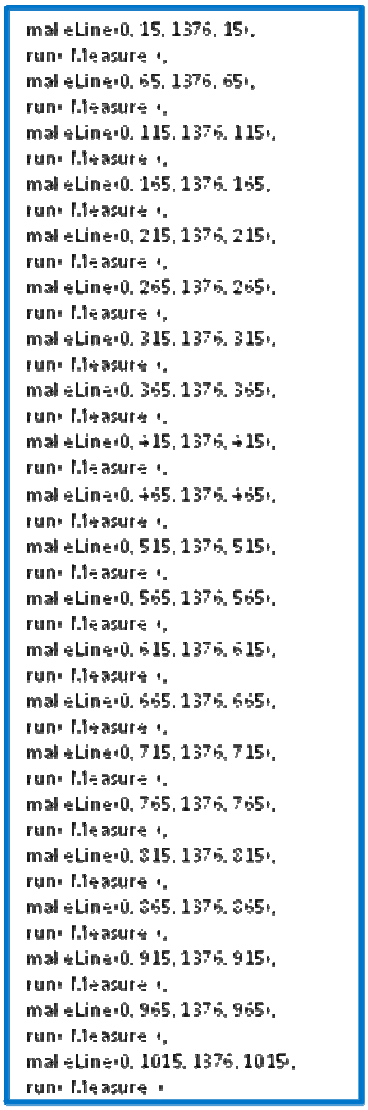

Figure 23: Coding for line scan MACRO in NIH ImageJ freeware. The coding was written to section each opened with 21 equidistant lines. The numerical values displayed by the "*makeLine*" command are the coordinates within the image that indicate the origin and end of each line. The "*Measure*" command instructs the program to take the mean grayscale intensity of all the objects each line crosses in its path from its origin to its end.

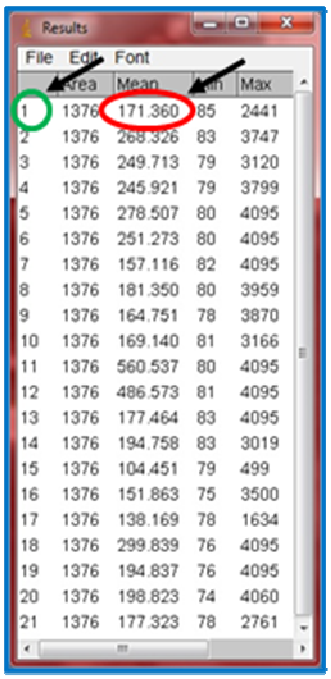

Figure 24: Results from line scan MACRO after it is applied to an opened image of the fluorescent microparticles. The black arrows point to the line identification number, circled in green, and the mean value of intensity obtained for that line, circled in red.

This process was repeated for both the $Ru(Ph_2phen_3)Cl_2$ and the Nile blue chloride fluorescence for all time points. The data was stored in a spreadsheet where all calculations regarding use of the two Stern-Volmer models and statistics were later performed. Figures 23 and 24 show the coding for the MACRO and the results summary given by ImageJ upon application of the MACRO to an opened image.

3. Image analysis protocols for measuring overall and area pEGFP-HIF-1α fusion intensities for tumor cell hypoxia experiments

In Chapter 5, we described the image analyses performed for the hypoxia experiments performed to three different tumor cell types transfected to express a

pEGFP-HIF-1α fusion. Two protocols were said to have been applied: (1) a line scan protocol for the determination of overall grayscale intensity and (2) a threshold protocol for the measurement of the pEGFP-HIF-1α fusion's occupied area and intensity. Images for these experiments were captured at 40x magnification. At this magnification, the length to pixel ratio is 0.16125 μm/pixel and the size of the total imaged area was 221.88 x 165.12 μm. The first protocol employed the exact same two protocols described in sections 1 and 2 of this Appendix, with the exception that an image of the pEGFP-HIF-1α fluorescence was analyzed instead. The values obtained for grayscale intensity at each time point were normalized to cell number as measured by the cell-counting MACRO when applied to the images of the DAPI stained cell nuclei for that same time point (see Figure 14a for results).

The second protocol however, employed a different method, which is to be described next. We began by opening an image of the pEGFP-HIF-1α fusion fluorescence for the desired time point. Then, a custom MACRO was applied to the image. This MACRO adjusted the image for selection of the areas within the image the software perceived as containing significant fluorescence by using the "*Threshold*" command. This command isolates areas of fluorescence and transforms the image into a projection of two solid colors, usually a combination of black and white or a combination of red and black. Figures 25 and 26 show the written MACRO for this protocol and the opened image of the pEGFP-HIF-1α fusion fluorescence and its corresponding threshold projection.

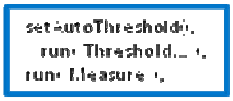

Figure 25: Coding for threshold MACRO in NIH ImageJ freeware. The coding was written to isolate the areas of fluorescence of the staining being investigated at the desired time point. The "*Measure*" command instructs the program to measure the collective area of all the isolated areas (in μm^2) and the total mean intensity of those areas.

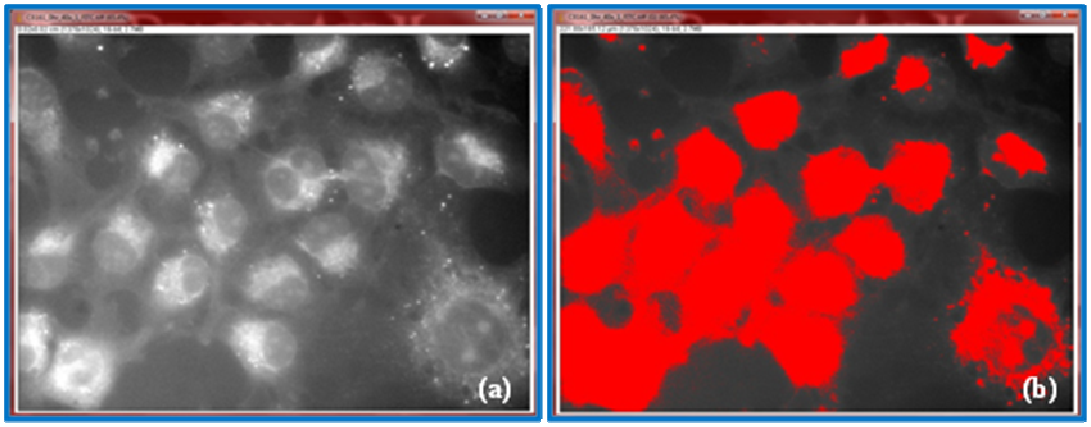

Figure 26: (a) Image of pEGFP-HIF-1α fluorescence from C8161 cells as opened by ImageJ. **(b)** Threshold image of pEGFP-HIF-1α fluorescence from C8161 cells as yielded by MACRO upon application to opened image. The areas in red shading are the areas chosen by the "*Threshold*" command as those containing fluorescence.

Results yielded from the application of the MACRO to the desired image were the tabulated. These were the total threshold area and its total intensity. Figure 27 displays the results summary given ImageJ upon application of the MACRO to the opened image.

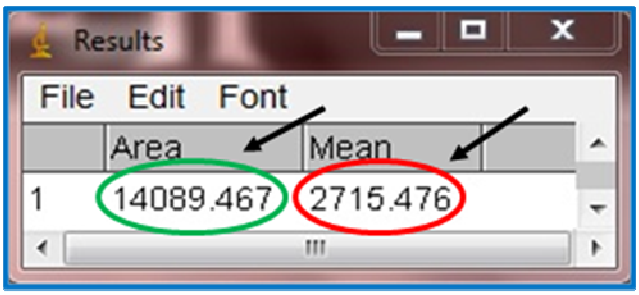

Figure 27: Results from threshold MACRO after it is applied to an opened image of pEGFP-HIF-1α fusion fluorescence. The black arrows point to the total measured area of fluorescence (in μm^2), circled in green, and the mean value of intensity for the total measured area, circled in red.

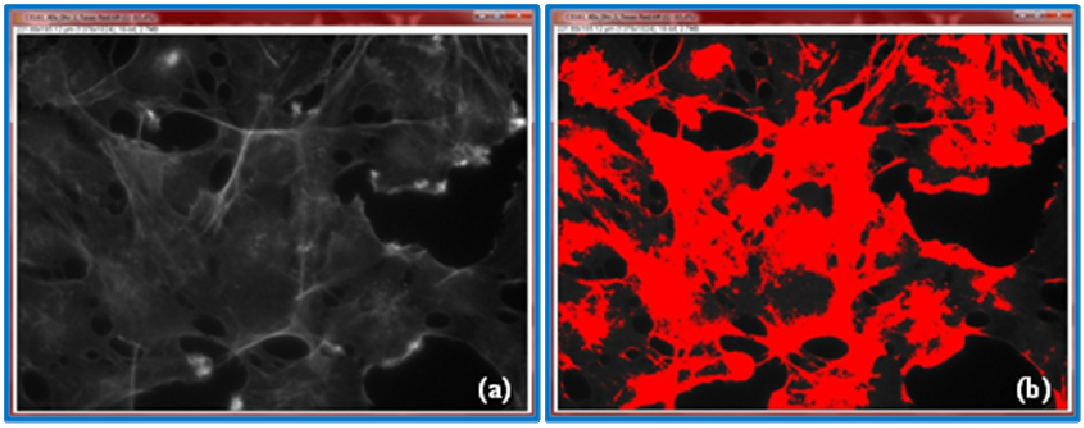

Figure 28: (a) Image of F-actin fluorescence from C8161 cells as opened by ImageJ. **(b)** Threshold image of F-actin fluorescence from C8161 cells as yielded by MACRO upon application to opened image. The areas in red shading are the areas chosen by the "*Threshold*" command as those containing fluorescence.

This same process was applied to the images captured for the F-actin staining. All data was stored in a spreadsheet where both values of occupied area of fluorescence and area intensity for pEGFP-HIF-1α and F-actin were normalized to cell number, as measured by the cell-counting MACRO, and the ratio between pEGFP-HIF-1α and F-actin area of fluorescence and intensity were obtained (see

Figures 14a and 14b for results). Figure 28 shows the opened image of the F-actin fluorescence and its corresponding threshold projection.

4. Closing statements

It is important to note that the results summarized upon application of each MACRO depend on those instructed to the program to display. To select which measurements you wish for the program to conduct, one must open the "*Set Measurements*" tab within the "*Analyze*" menu on the ImageJ interface. When the new menu opens, select which measurements to conduct. Some examples of measurements the program can conduct are mean gray intensity, minimum and maximum intensity, area, perimeter, centroid, and kurtosis among many others. This selection must be performed before any analysis is done in order to ensure the correct measurements are performed. Finally, one must always make sure that the "*Limit to threshold*" option is selected when conducting measurements that require threshold of an image. Otherwise, conducted measurements will not be accurate, as they will account for the entire image rather than the areas selected by the "*Threshold*" command.

REFERENCES

1. Wong, J.Y., J.B. Leach, and X.Q. Brown, Balance of chemistry, topography, and mechanics at the cell-biomaterial interface: Issues and challenges for assessing the role of substrate mechanics on cell response. Surface Science, 2004. 570: p. 119-133.
2. Gunawan, R.C., et al., Cell migration and polarity on microfabricated gradients of extracellular matrix proteins. Langmuir, 2006. 22(9): p. 4250-8.
3. Shuler, M.L. and F. Kargi, Bioprocess Engineering: Basic Concepts. 2nd edition, 2002: Prentice Hall.
4. Martin, Y. and P. Vermette, Bioreactors for tissue mass culture: Design, characterization, and recent advances. Biomaterials, 2005. 26(35): p. 7481-503.
5. Radisic, M., et al., Oxygen gradients correlate with cell density and cell viability in engineered cardiac tissue. Biotechnology and Bioengineering, 2006. 93(2): p. 332-43.
6. Tilles, A.W., et al., Effects of oxygenation and flow on the viability and function of rat hepatocytes cocultured in a microchannel flat-plate bioreactor. Biotechnology and Bioengineering, 2001. 73(5): p. 379-89.
7. O'Driscoll, S.W., J.S. Fitzsimmons, and C.N. Commisso, Role of oxygen tension during cartilage formation by periosteum. Journal of Orthopeadic Research, 1997. 15(5): p. 682-7.

8. Martin, H., et al., Morphological and biochemical integrity of human liver slices in long-term culture: effects of oxygen tension. Cell Biology Toxicology, 2002. 18(2): p. 73-85.

9. Bussink, J., et al., Optical sensor-based oxygen tension measurements correspond with hypoxia marker binding in three human tumor xenograft lines. Radiation Research, 2000. 154(5): p. 547-55.

10. Fariss, M.W., Oxygen toxicity: unique cytoprotective properties of vitamin E succinate in hepatocytes. Free Radical Biology & Medicine, 1990. 9(4): p. 333-43.

11. Moeller, B.J., R.A. Richardson, and M.W. Dewhirst, Hypoxia and radiotherapy: opportunities for improved outcomes in cancer treatment. Cancer Metastasis Reviews, 2007. 26(2): p. 241-8.

12. Dewhirst, M.W., Y. Cao, and B. Moeller, Cycling hypoxia and free radicals regulate angiogenesis and radiotherapy response. National Reviews: Cancer, 2008. 8(6): p. 425-37.

13. Rzymski, T. and A. Harris, The unfolded protein response and integrated stress response to anoxia. Clinical Cancer Research, 2007. 13(9): p. 2537-2540.

14. Anderson, P. and N. Kedersha, Stressful initiations. Journal of Cell Science, 2002. 115(16): p. 3227-3234.

15. Papandreou, I., et al., Anoxia is necessary for tumor cell toxicity caused by a low-oxygen environment. Cancer Research, 2005. 65: p. 3171-3178.

16. Chu, V., et al., *Staphylococcus aureus* bacteremia in patients with prosthetic devices: costs and outcomes. America Journal of Medicine, 2005. 118(12): p. 1416.

17. Gotz, F., *Staphylococcus* and biofilms. Molecular Microbiology, 2002. 43(6): p. 1367-1378.

18. Stewart, P. and J. Costerton, Antibiotic resistance of bacteria in biofilms. Lancet, 2001. 358(9276): p. 135-138.

19. Folkesson, A., et al., Biofilm Induced Tolerance towards Antimicrobial Peptides. Plos One, 2008: ARTN e1891. DOI 10.1371.

20. Lesens, O., et al., Positive surveillance blood culture is a predictive factor for secondary metastatic infection in patients with *Staphylococcus aureus* bacteraemia. Journal of Infection, 2004. 48(3): p. 245-252.

21. Cramton, S., et al., Anaerobic conditions induce expression of polysaccharide intercellular adhesin in *Staphylococcus aureus* and *Staphylococcus epidermidis*. Infection and Immunity, 2001. 69(6): p. 4079-85.

22. Vaupel, P., The role of hypoxia-induced factors in tumor progression. Oncologist, 2004. 9 Suppl 5: p. 10-7.

23. Ke, Q. and M. Costa, Hypoxia-inducible factor-1 (HIF-1). Molecular Pharmacology, 2006. 70(5): p. 1469-80.

24. Zhong, H., et al., Overexpression of hypoxia-inducible factor 1α in common human cancers and their metastases. Cancer Research, 1999. 59(22): p. 5830-5.

25. Vaupel, P., F. Kallinowski, and P. Okunieff, Blood flow, oxygen and nutrient supply, and metabolic microenvironment of human tumors: a review. Cancer Research, 1989. 49(23): p. 6449-65.

26. Acker, T. and K.H. Plate, Role of hypoxia in tumor angiogenesis-molecular and cellular angiogenic crosstalk. Cell & Tissue Research, 2003. 314(1): p. 145-55.

27. Belozerov, V.E. and E.G. Van Meir, Hypoxia inducible factor-1: a novel target for cancer therapy. Anticancer Drugs, 2005. 16(9): p. 901-9.

28. Blagosklonny, M.V., Hypoxia-inducible factor: Achilles' heel of antiangiogenic cancer therapy (review). International Journal of Oncology, 2001. 19(2): p. 257-62.

29. Nahmias, Y., et al., A novel formulation of oxygen-carrying matrix enhances liver-specific function of cultured hepatocytes. FASEB Journal, 2006. 20(14): p. 2531-3.

30. Gordon, J. and A.F. Palmer, Impact of increased oxygen delivery via bovine red blood cell supplementation of culturing media on select metabolic and synthetic functions of C3A hepatocytes maintained within a hollow fiber bioreactor. Artificial Cells, Blood Substitutes, Immobilization Biotechnology, 2005. 33(3): p. 297-306.

31. Brown, D.A., et al., Analysis of oxygen transport in a diffusion-limited model of engineered heart tissue. Biotechnology and Bioengineering, 2007. 97(4): p. 962-75.

32. Chin, K., et al., Hydrogel-Perfluorocarbon Composite Scaffold Promotes Oxygen Transport to Immobilized Cells. Biotechnology Progress, 2008. 24(2): p. 358-366.

33. Ju, L.-K. and C.S. Ho, The Measurement of Oxygen Diffusion Coefficients in Polymeric Solutions. Chemical Engineering Science, 1986. 41(3): p. 579-589.

34. Hulst, A.C., et al., Determination of the Effective Diffusion Coefficient of Oxygen in Gel Materials in Relation to gel Concentration. Biotechnology Techniques, 1989. 3(3): p. 199-204.

35. Li, R.H., D.H. Altreuter, and F.T. Gentile, Transport Characterization of Hydrogel Matrices for Cell Encapsulation. Biotechnology and Bioengineering, 1996. 50: p. 365-373.

36. Kurosawa, H., M. Matsumura, and H. Tanaka, Oxygen Diffusivity in Gel Beads Containing Viable Cells. Biotechnology and Bioengineering, 1989. 34: p. 926-932.

37. Sun, Y., et al., Diffusivity of Oxygen into Carriers Entrapping Whole Cells. Biotechnology and Bioengineering, 1989. 34: p. 55-58.

38. Hiemstra, H., L. Dijkhuizen, and W. Harder, Diffusion of Oxygen in Alginate Gels Related to the Kinetics of Methanol Oxidation by Immobilized Hansenula polymorpha Cells. European Journal of Applied Microbiology and Biotechnology, 1983. 18: p. 189-196.

39. Parker, J.W. and M.E. Cox, Mass Transfer of Oxygen in Poly(2-Hydroxyethyl Methacrylate). Journal Polymer Science, Part A: Polymer Chemistry, 1988. 26: p. 1179-1188.

40. Malda, J., et al., Oxygen gradients in tissue-engineered PEGT/PBT cartilaginous constructs: measurement and modeling. Biotechnology and Bioengineering, 2004. 86(1): p. 9-18.

41. Sullivan, J.P., J.E. Gordon, and A.F. Palmer, Simulation of oxygen carrier mediated oxygen transport to C3A hepatoma cells housed within a hollow fiber bioreactor. Biotechnology and Bioengineering, 2006. 93(2): p. 306-17.

42. Radisic, M., et al., Mathematical model of oxygen distribution in engineered cardiac tissue with parallel channel array perfused with culture medium containing oxygen carriers. American Journal Physiology: Heart and Circulatory Physiology, 2005. 288(3): p. H1278-89.

43. Croll, T.I., et al., Modelling Oxygen Diffusion and Cell Growth in a Porous, Vascularising Scaffold for Soft Tissue Engineering Applications. Chemical Engineering Science, 2005. 60: p. 4924-4934.

44. Allen, J.W. and S.N. Bhatia, Formation of steady-state oxygen gradients in vitro: application to liver zonation. Biotechnology and Bioengineering, 2003. 82(3): p. 253-62.

45. Ljungkvist, A.S., et al., Vascular architecture, hypoxia, and proliferation in first-generation xenografts of human head-and-neck squamous cell carcinomas. International Journal of Radiation Oncology, Biology, and Physics, 2002. 54(1): p. 215-28.

46. Miller, G.G., et al., Quantitation of hypoxia in multicellular spheroids by video image analysis. International Journal of Radiation Oncology, Biology, and Physics, 1989. 16(4): p. 949-52.

47. Kellner, K., et al., Determination of oxygen gradients in engineered tissue using a fluorescent sensor. Biotechnology and Bioengineering, 2002. 80(1): p. 73-83.

48. Moriyama, E.H., et al., In Vitro Influence of Hypoxia on Bioluminescence Imaging in Brian Tumor Cells. Proceedings of the SPIE, 2007. 6449: p. 6449F1-6449F8.

49. Williams, S.N.O., R.M. Callies, and K.M. Brindle, Mapping oxygen tension and cell distribution in a hollow-fiber bioreactor using magnetic resonance imaging. Biotechnology and Bioengineering, 1997. 56(1): p. 56-61.

50. Vinogradov, S.A., et al., Noninvasive imaging of the distribution in oxygen in tissue in vivo using near-infrared phosphors. Biophysics Journal, 1996. 70(4): p. 1609-17.

51. Bratasz, A., et al., In vivo imaging of changes in tumor oxygenation during growth and after treatment. Magnetic Resonance in Medicine, 2007. 57(5): p. 950-9.

52. Revsbech, N.P., An Oxygen Microsensor with a Guard Cathode. Limnology and Oceanography, 1989. 34(2): p. 474-478.

53. Lakowicz, J.R., Principles of Fluorescence Spectroscopy. 3rd edition, 2006: Springer.

54. Demas, J.N. and B.A. DeGraff, Interactions of Transition-Metal-Complex Photosensitizers with Polymers and Organized Media. Journal of Macromolecular Science, Chemistry, 1988. A25(10-11): p. 1189-1214.

55. Demas, J.N. and B.A. DeGraff, Applications of highly luminescent transition metal complexes in polymer systems. Makromolekulare Chemie. Macromolecualr Symposia, 1992. 59: p. 35-51.

56. Xu, W., et al., Oxygen sensors based on luminiscence quenching: interactions of metal complexes with the polymer supports. Analytical Chemistry, 1994. 66: p. 4133-4141.

57. Kneas, K.A., et al., Oxygen sensors based on luminescence quenching: Interaction of tris(4,7-diphenyl-1,10-phenanthroline)ruthenium(II) chloride and pyrene with polymer supports. Applied Spectroscopy, 1997. 51(9): p. 1346-1351.

58. Carraway, E.R., et al., Photophysics and photochemistry of oxygen sensors based on luminescent transition-matel complexes. Analytical Chemistry, 1991. 63: p. 337-342.

59. Brasuel, M., et al., Production, characteristics, and applications of fluorescent PEBBLE nanosensors: Potassium, oxygen, calcium, and pH imaging inside live cells. Sensors and Materials, 2002. 14(6): p. 309-338.

60. Ge, X., et al., Validation of an optical sensor-based high-throughput bioreactor system for mammalian cell culture. Journal of Biotechnology, 2006. 122(3): p. 293-306.

61. John, G.T., et al., Integrated optical sensing of dissolved oxygen in microtiter plates: A novel tool for microbial cultivation. Biotechnology and Bioengineering, 2003. 81(7): p. 829-836.

62. McDonagh, C., B.D. MacCraith, and A.K. McEvoy, Tailoring of Sol-Gel films for optical sensing of oxygen in gas and aqueous phase. Analytical Chemistry, 1998. 70: p. 45-50.

63. Klimant, I., V. Meyer, and M. Kuhl, Fiber-optic oxygen microsensors: A new tool in aquatic biology. Limnology and Oceanography, 1995. 40(6): p. 1159-1165.

64. Klimant, I., et al., Fast Response Oxygen Micro-Optodes Based on Novel Soluble Ormosil Glasses. Mikrochimica Acta, 1999. 131: p. 35-46.

65. Wolfbeis, O.S., Fiber-optic chemical sensors and biosensors. Analytical Chemistry, 2006. 78(12): p. 3859-74.

66. Stöber, W., A. Fink, and E. Bohn, Controlled growth of monodisperse silica spheres in the micron size range. Journal of Colloid and Interface Science, 1968. 26: p. 62-69.

67. Karmakar, B., et al., Silica microspheres from the system tetraethylorthosilicate-acetic acid-water. Journal of Non-Crystalline Solids, 1991. 135: p. 29-36.

68. Karmakar, B., G. De, and D. Ganguli, Dense silica microspheres from organic and inorganic acid hydrolisis of TEOS. Journal of Non-Crystalline Solids, 2000. 272: p. 119-126.

69. Xu, Y., et al., A new study on the kinetics of Stöber synthesis by in-situ liquid ^{29}Si NMR. Journal of Sol-Gel Science and Technology, 2007. 42: p. 13-20.

70. Rossi, L., et al., Stober synthesis of monodispersed luminescent silica nanoparticles for bioanalytical assays. Langmuir, 2005. 21(10): p. 4277-4280.

71. Nagao, D., et al., Synthesis of highly monodisperse particles composed of a magnetic core and fluorescent shell. Langmuir, 2008. 24(1): p. 9804-9808.

72. Anderson, K.R., T.M. Obey, and B. Vincent, Surfactant-stabilized silicone oil-in-water emulsions. Langmuir, 1994. 10 (7): p. 2493-2494.

73. Goller, M.I., et al., Inorganic "silicone oil" microgels. Colloids and Surfaces A: Physicochemical and Engineering Aspects, 1997. 123-124: p. 183-193.

74. Rossi, L., et al., Fluorescent silica nanospheres for digital counting bioassay of the breast cancer marker HER2/nue. Biosensors & Bioelectronics, 2006. 21(10): p. 1900-1906.

75. Gao, D., et al., Resonance Energy Transfer-Amplifying Fluorescence Quenching at the Surface of Silica Nanoparticles toward Ultrasensitive Detection of TNT. Analytical Chemistry, 2008. 80(1): p. 8545-8553.

76. Neumann, B., et al., Stability of various silicone oil/water emulsion films as a function of surfactant and salt concentration. Langmuir, 2004. 20(1): p. 4336-4344.

77. Brown, J.Q., R. Srivastava, and M.J. McShane, Encapsulation of glucose oxidase and an oxygen-quenched fluorophore in polyelectrolyte-coated calcium alginate microspheres as optical glucose sensor systems. Biosensors & Bioelectronics, 2005. 21(1): p. 212-6.

78. Vasylevska, G.S., et al., Indicator-Loaded Permeation-Selective Microbeads for Use in Fiber Optic Simultaneous Sensing of pH and Dissolved Oxygen. Chemistry of Materials, 2006. 18: p. 4609-4616.

79. Munn, L.L., R.J. Melder, and R.K. Jain, Analysis of cell flux in the parallel plate flow chamber: implications for cell capture studies. Biophysics Journal, 1994. 67(2): p. 889-95.

80. Bacon, J.R. and J.N. Demas, Determination of oxygen concentrations by luminescence quenching of a polymer-immobilized transition metal complex. Analytical Chemistry, 1987. 59: p. 2780-2785.

81. McDonald, J.C., et al., Fabrication of microfluidic systems in poly(dimethylsiloxane). Electrophoresis, 2000. 21(1): p. 27-40.

82. Charati, S.G. and S.A. Stern, Diffusion of gases in silicone polymers: Molecular dynamics simulations. Macromolecules, 1998. 31: p. 5529-5535.

83. Xu, H., et al., A real-time ratiometric method for the determination of molecular oxygen inside living cells using sol-gel-based spherical optical nanosensors with applications to rat C6 glioma. Analytical Chemistry, 2001. 73(17): p. 4124-33.

84. Borisov, S.M. and I. Klimant, Ultrabright oxygen optodes based on cyclometalated iridium(III) coumarin complexes. Analytical Chemistry, 2007. 79(19): p. 7501-9.

85. Han, B.-H., I. Manners, and M.A. Winnik, Oxygen sensors based on mesoporous silica particles on layer-by-layer self-assembled films. Chemistry of Materials, 2005. 17(12): p. 3160-3171.

86. Lebedev, A., et al., Dendritic Phosphorescent Probes for Oxygen Imaging in Biological Systems. Acs Applied Materials & Interfaces, 2009. 1(1): p. 1292-1304.

87. Acosta, M., et al., Fluorescent microparticles for sensing cell microenvironment oxygen levels within 3D scaffolds. Biomaterials, 2009. 30(17): p. 3068-74.

88. Lee, M., F. Beyer, and E. Furst, Synthesis of monodisperse fluorescent core-shell silica particles using a modified Stober method for imaging individual particles in dense colloidal suspensions. Journal of Colloid and Interface Science, 2005. 288(1): p. 114-123.

89. Patti, J.M., et al., The Staphylococcus aureus collagen adhesin is a virulence determinant in experimental septic arthritis. Infection and Immunity, 1994. 62(1): p. 152-61.

90. Wang, G.L., et al., Hypoxia-inducible factor 1 is a basic-helix-loop-helix-PAS heterodimer regulated by cellular O_2 tension. Proceedings of the National Academy of Sciences (PNAS, USA), 1995. 92(12): p. 5510-4.

91. Wotzlaw, C., et al., Optical analysis of the HIF-1 complex in living cells by FRET and FRAP. FASEB Journal, 2007. 21(3): p. 700-7.

92. Liu, X.H., et al., Prostaglandin E2 induces hypoxia-inducible factor-1alpha stabilization and nuclear localization in a human prostate cancer cell line. Journal of Biological Chemistry, 2002. 277(51): p. 50081-6.

93. Genetos, D.C., et al., Oxygen tension modulates neurite outgrowth in PC12 cells through a mechanism involving HIF and VEGF. Journal of Molecular Neuroscience, 2010. 40(3): p. 360-6.

94. Kim, H.L., et al., A domain responsible for HIF-1alpha degradation by YC-1, a novel anticancer agent. International Journal of Oncology, 2006. 29(1): p. 255-60.

95. Mitra, S., et al., Photodynamic therapy mediates the oxygen-independent activation of hypoxia-inducible factor 1alpha. Molecular Cancer Therapy, 2006. 5(12): p. 3268-3274.

96. Lucarini, G., et al., Increased VEGF165 expression in HCT116 colon cancer cells after transient transfection with a GFP vector encoding HIF-1 gene. Journal of Experimental & Clinical Cancer Research, 2007. 26(4): p. 515-519.

97. Chachami, G., et al., Transport of hypoxia-inducible factor HIF-1 alpha into the nucleus involves importins 4 and 7. Biochemical and Biophysical Research Communications, 2009. 390(2): p. 235-240.